Orientation dependent deformation by slip and twinning in magnesium during single crystal indentation

C. Zambaldi,* C. Zehnder and D. Raabe

MPI für Eisenforschung, Düsseldorf, Germany

Received 18 August 2014; revised 3 December 2014; accepted 6 January 2015

Abstract—We present the orientation dependent indentation response of pure magnesium during single grain indentation. A conical indenter and maximum loads between 50 mN and 900 mN were employed. Indent topographies were acquired by confocal microscopy. The indents were also characterized by electron backscatter orientation microscopy for their microstructures. Pronounced activation of specific twinning systems was observed around the impressions. The resulting data were compiled into the inverse pole figure presentation of indent microstructures and topographies after Zambaldi and Raabe, Acta Mater. (2010). Three-dimensional crystal plasticity finite element simulation of the indentation deformation supports the interpretation of the orientation dependent slip and twinning patterns around the indents. The match between the activation of observed and simulated twinning variants is discussed with respect to the conditions for nucleation and growth of extension twins. Furthermore, the compatibility of the twinning strains with the imposed deformation is discussed based on the expanding cavity model of indentation. The orientation dependent response of magnesium during indentation is compared to the literature data for indentation of alpha-titanium and beryllium. Recommendations are given on how to exploit the characteristic nature of the observed indentation patterns to rapidly assess the relative activity of deformation mechanisms and their critical shear stresses during alloy development.
© 2015 Acta Materialia Inc. Published by Elsevier Ltd. All rights reserved.

Keywords: Indentation; Twinning; Nucleation; EBSD; Anisotropy

1. Introduction

1.1. General introduction and state of micromechanical models for magnesium

Magnesium alloys are an attractive class of structural materials [1–4]. Their widespread application is currently hampered by the low ductility of many available alloys at room temperature. The goal to increase the use of light-weight materials in structural applications has lead to an increased interest in magnesium wrought alloys in the recent years.

The addition of small amounts of rare earth elements or lithium improves the forming potential of these alloys [5–8]. The understanding of this ductilizing effect advanced considerably in the recent years [9–13]. A method to efficiently quantify the strength of this effect, specifically regarding the change in the relative activation of different types of slip and twinning systems for variations in rare earth contents, could support and even guide the alloy design process.

Due to the pronounced twinning which is commonly observed during the plastic deformation of magnesium, new interest was also triggered for an improved understanding of this deformation mechanism. Furthermore, micromechanical models have progressed and started to incorporate physically-based twinning models [14]. However, these formulations need accurate and physically meaningful parameters to calibrate their internal twin nucleation and growth models. Even if some of the relevant parameters can be predicted by ab initio or molecular dynamics studies [15,12,16], the resulting predictions need to be validated by targeted experiments.

Understanding the mechanisms of twin formation in hexagonal metals is a long-standing problem. Despite the increased amount of research, several key issues have not been resolved yet and a better understanding and quantification of the competition between the predominant deformation mechanisms is necessary to develop improved alloying concepts. Based on current characterization techniques a number of studies have been carried out to clarify the micromechanical processes [17,18] as well as statistical variations [19,20] of the twinning process in hexagonal close packed crystals.

One of the major challenges in the study of twin formation is that the location where a twin will form is generally not known beforehand. Also the growth of twins is fast once a viable nucleus has been formed [21]. Therefore, the initial stages of twinning are very difficult to investigate by experiments. Recently a combination of molecular dynamics simulation and electron backscatter diffraction

* Corresponding author; e-mail: c.zambaldi@mpie.de

(EBSD) crystal orientation mapping was used to study twin nucleation at grain boundaries in magnesium [19].

The often observed, extended and wedge-like morphology of deformation twins in magnesium cannot readily be incorporated into finite element based simulations. Current research of Glüge et al. [22], Zhang and Joshi [23] and Abdolvand and Daymond [24] shows some promising results on this problem. Most of the literature, however, uses a homogenized formulation for the twinned volume [25–28].

Phase field models have been adapted most recently to represent the kinetics of twin nucleation and growth in a spatially resolved manner [29–32]. The resulting models were applied to indentation-induced twinning of calcite and sapphire [30] and NiAl [32], as well as to crack-induced twinning in magnesium [31].

We develop in this study one possible prerequisite to the problem of calibrating such emerging micromechanical models. Based on the reproducible generation of twins by single-crystal indentation, the resulting microstructures can be easily compared to simulation results. Correspondingly, the models could be validated against these experiments.

1.2. Motivation: limitations of the existing tools to determine relative activation of deformation systems

The most pragmatic way to study micromechanical processes in magnesium is to analyze the microstructure of a polycrystal after deformation. The main advantage of this method is the immediate relevance of the findings to the deformation of wrought alloys. The main drawback of this approach is the multitude of mechanisms that are operating at the same time which makes it difficult to isolate their exact nature. Also, the strong flow anisotropy of individual crystals in magnesium results in a rather heterogeneous local stress field even during homogeneous external loading. Often a complex three-dimensional stress state will be present inside the microstructures. Under these conditions each grain's plastic deformation is of unique character and depends on its immediate surroundings. Owing to these non-homogeneous stress and strain fields, any experimental work in polycrystalline material that does not quantify the deformation mechanisms with good statistics will fail to extract general knowledge. Similarly, any characterization method for polycrystalline materials that does not take into account the third dimension will not be able to explain the observed deformation structures at the surface because of the effects from the material beneath it [24].

Further, the simulation of deformation textures has been applied to the problem of indirectly identifying the predominant slip systems in magnesium through the asymmetric portions of the deformation gradient, causing crystal rotation [6]. While this approach has the advantage to be based on the technologically relevant case of polycrystalline deformation, its drawback consists in the lack of appropriate models to describe the complex deformation of (hcp) metals especially when twinning deformation is present. Also, crystal rotations, i.e. texture evolution, does not always relate to the activated shear systems in a unique fashion. Hence, despite large efforts, no fully satisfying crystal plasticity model is available for magnesium because of the difficulty to link the length scales of microscopic

twinning and polycrystal deformation as modeled by the crystal plasticity finite element method (CPFEM).

The relative activity of deformation systems has also been studied by X-ray diffraction experiments [33]. Further volume characterization of deformation processes in magnesium and other hexagonal metals was carried out by 3D X-ray diffraction [34,35] and 3D-EBSD [36].

To isolate the contributions from different deformation mechanisms to the overall strain and the changes in the microstructure, it is desirable to perform single crystal deformation experiments in addition to the mechanical testing of polycrystals. Besides the indentation of single crystals that will be presented here, other kinds of micromechanical experiments have been performed in the past [37–43] such as the deformation by channel die plane strain compression [39–41] or micropillar compression experiments [42,43]. They are discussed and compared in more detail in Section 5.11.

1.3. Crystal plasticity of magnesium

Pure magnesium deforms mainly by basal slip along the $\langle a \rangle$-directions and extension twinning of type $\{10\bar{1}2\}$ $\langle\bar{1}100\rangle$ [37,44,39,45]. It is not clear, however, whether these two types of deformation systems can accommodate arbitrary three-dimensional strain [46,47]. Occasionally the activation of additional slip systems is energetically more favorable and dislocation glide on prismatic and pyramidal systems as well as compression twinning [40,41] have been observed.

Hutchinson and Barnett [45] compiled the literature on experiments conducted on single crystals of pure magnesium and Mg-based alloys and the critical resolved shear stress (CRSS) values derived from them. In magnesium the high ratios between the CRSS values for hard and soft deformation modes largely prevent the harder deformation mechanisms from operating.

Stohr and Poirier [48] have investigated the activation of a second order pyramidal slip in Magnesium. They have reported a minimum of its CRSS around room temperature. Jones and Hutchinson [49] discussed the primary slip systems and dislocation mechanisms of many hexagonal metals.

1.3.1. Twin nucleation
General summaries of the nature of twinning and twin nucleation were given by Christian and Mahajan [50] and Yoo [47]. Aydiner et al. [51] have studied the nucleation of twin variants in an AZ31 alloy during compression of a polycrystal by in situ 3D-XRD. Barrett et al. [52] have studied the Schmid-factor dependency of twin nucleation by molecular dynamics simulation. Abdolvand and Daymond [24] investigated the spatial distribution of twinning in a magnesium polycrystal by crystal plasticity simulations. Yu et al. [53] have reported a size effect on deformation twinning for compression of microcolumns with square cross-sections. This phenomenon has also been discussed by El Kadiri et al. [54].

1.3.2. Twin variant selection
The formation of specific twin variants has been shown to significantly deviate from predictions based on a macroscopic Schmid-factor in several cases [55–59]. Some authors

attributed the variant selection mainly to the plastic compatibility of the neighboring grains [56,57].

Building on these previous and own observations, Beyerlein and Tomé [60] presented a probabilistic twin nucleation model based on statistical observation of twinning in polycrystalline magnesium.

1.4. Indentation of hexagonal crystals

Twinning has been reported previously for the indentation of hexagonal materials [61–66,18,67]. However, non-axisymmetric indenters with sharp edges such as Vickers or Berkovich geometries were employed in most of the experimental work. These indenter geometries usually make a thorough analysis of the deformation processes difficult unless the edges of the tool have been carefully aligned with specific crystallographic directions.

The phenomenon of indentation induced twinning was already observed by Tammann and Müller [61] in zinc. Only later the forming lamellae were interpreted in terms of their crystallographic origin [63,64,66].

Reed-Hill and Robertson [62] have observed six sets of twins around an indentation with a ball of 1.6 mm diameter into the basal plane of pure magnesium. Twinning structures similar to the ones presented in this work have been observed in magnesium by Kim [18] under a flat punch indentation along $[2\bar{1}\bar{1}2]$.

Tsuya [65] has presented images of Knoop and Vickers indents in beryllium at different temperatures. The observed indent microstructures changed from showing slip and twinning to pure dislocation glide for increased temperatures. Blish [66] performed Berg-Barrett X-ray imaging for indents in zinc and discussed the resulting features from slip and twinning around the indentations. Basu and Barsoum [68] have shown how pyramidal and basal deformation mechanisms affect the indentation topographies for different crystallographic orientations of hexagonal ZnO crystals. Later they have illustrated the extension of basal dislocation loops under a spherical indenter in ZnO [69].

Zambaldi et al. [70] have extracted CRSS values from spherical nanoindentation of alpha-titanium. By inverse modeling of the indentation process the parameters of a phenomenological crystal plasticity model were identified based on the orientation dependent impression topographies and on the load–displacement curves. During this small-scale indentation in titanium no twinning was observed around the indents.

Cho et al. [67] have reported twinning around Vickers indents in the magnesium alloy ZK60.

Recently, Somekawa and Schuh [71] have presented cross sections through twin microstructures under cube-corner indentation in high purity and alloyed magnesium with a coarse grain structure. Shin et al. [72] have also observed twinning around Berkovich indentations into basal and second order prismatic planes of magnesium. They identified twin-favorable regions around such indentations.

Kitahara et al. [73] have presented the indentation response of high symmetry orientations of pure magnesium single crystals. They used a 1 mm steel ball as indenter and combined light optical microscopy with EBSD orientation mapping and CPFEM simulations to characterize and interpret the resulting microstructures. Very recently also Selvarajou et al. [74] have reported indentation experiments

and corresponding CPFEM simulations on the basal and prismatic planes of pure magnesium.

1.5. Outline

Here we investigate the plastic deformation mechanisms of single crystal magnesium by microindentation with sharp conical tip geometries. These indentation experiments are able to capture the single crystal deformation behavior in a comprehensive and reproducible manner.

First some representative indent microstructures from a large number of conical microindentations in pure magnesium are presented. The orientation dependence of the indent microstructures is shown in the inverse pole figure representation of indent microstructures. Then the identification of different twin variants based on measured orientations, trace analysis and analysis of the twinning strains is discussed. Additionally, 3D-CPFEM simulations are carried out to quantify the contributions of competing deformation mechanisms to the overall deformation during indentation of magnesium. At last the simulation results are compared to the experimental findings and discussed with regard to the formation of specific twin variants around the indentations.

2. Experimental methods

2.1. Material and preparation

High purity magnesium (Mg > 99.98 wt.%[1]) in as-cast state was annealed at 450 °C for 20 h in (Ar/H_2) atmosphere and water-cooled in order to coarsen the microstructure. The material exhibited almost random texture with an average grain size of about 3 mm. Samples with approximate dimensions of 15 mm × 20 mm and a height of 6 mm were cut from the ingot by wire erosion. They were ground carefully with 2500 and 4000 grit SiC paper and electrolytically polished with *AC2 soft* (*Struers*) electrolyte at −10 °C and 30 V for 9 min and cleaned with ethanol and a 1% nital solution. Large area EBSD maps of the electropolished areas were acquired to determine the grain orientations for each sample.

2.2. Details of indentation experiments

Five samples were indented using a FischerScope microhardness tester. A custom-made sphero-conical diamond tool (Synton-MDP) with a nominal tip radius of 1 μm and a cone angle of 90° was used. Several arrays of indents were defined on each sample. Maximum loads of 50 mN, 100 mN, 200 mN, 300 mN and 900 mN resulted in indent diameters of up to around 50 μm (for 900 mN). Most indents were made with a maximum force of 300 mN. Loading to the maximum force was carried out in 20 equal increments at a rate of one increment per second. After reaching the maximum load the unloading was performed in the same 20 increments and at the same rate.

All indents were labeled based on three identifiers for the (1) sample, (2) indentation array and (3) number or

row/column index inside the respective array. These unique labels of the form ⟨sample⟩-⟨array⟩-⟨indent⟩, e.g. 4-0-(2,1) referring to an indentation in sample 4, indentation array 0, indent in row 2, column 1, are used throughout the text and figures to allow for convenient reference to the exact orientations and other data as given in Appendix, Table A.4.

2.3. Characterization of the indents

The indents were characterized in a field-emission gun (FEG) scanning electron microscope (SEM) at 15 kV acceleration voltage. Because of the statistical nature of twinning, backscatter electron (BSE) images were collected on at least five indents for each of several orientations. Additionally, EBSD orientation mapping with a step size of 0.5 μm was performed for one or more indents per array. To minimize topographic shadowing effects during EBSD pattern acquisition, the trace direction of the basal plane was approximately aligned with the direction perpendicular to the 70° tilt axis. Additionally, a second polishing step was applied on one sample to characterize the sub-surface twin microstructures. The topographies of selected indents were observed with a confocal white-light microscope (Nanofocus musurf).

3. Experimental results

3.1. Orientation dependent indent topographies and hardness anisotropy

Fig. 1 reproduces the topography of an indent made with a maximum load of 900 mN along a direction 14° away from the crystallographic ⟨c⟩-axis, or $[0\,0\,0\,1]$ in Miller–Bravais notation. The impression has an approximate diameter of 45 μm and a depth of about 22 μm. A maximum pile-up height of approximately 2 μm was observed in this case. Six pile-up features are visible in the topography and display variable amounts of twin-shaped surface features.

The measured pile-up topographies throughout the orientation space of magnesium are given in Fig. 2 for indents carried out with a maximum load of 300 mN. The in-plane orientation of the topographies follows the convention defined in Zambaldi and Raabe [75]. This convention removes one degree of freedom from the parameterization of the crystallographic orientation. The studied orientations can thus be described in terms of the two spherical polar coordinates, ζ and η, instead of their full Euler angles. In the remaining text the indented orientations are identified by these two angles with η referring to the polar or zenith angle, i.e. the angular distance from the ⟨c⟩-axis, and ζ referring to the azimuthal angle, i.e. the angular distance from the $[2\,\bar{1}\,\bar{1}\,0]$ direction, a_1, for a rotation around the ⟨c⟩-axis. Angle η between the ⟨c⟩-axis and the indentation direction ranges between 0° for ⟨c⟩-axis indentation and 90° for indentation directions in the basal plane. Angle ζ has a value range between 0° and 60°. Also, spatial features of the indents are in the following sometimes referred to as being located on the "inner" or "outer" side of the indents, where "inner" refers to the direction towards the ⟨c⟩-axis pole in the normal direction inverse pole figure (ND-IPF) illustration.

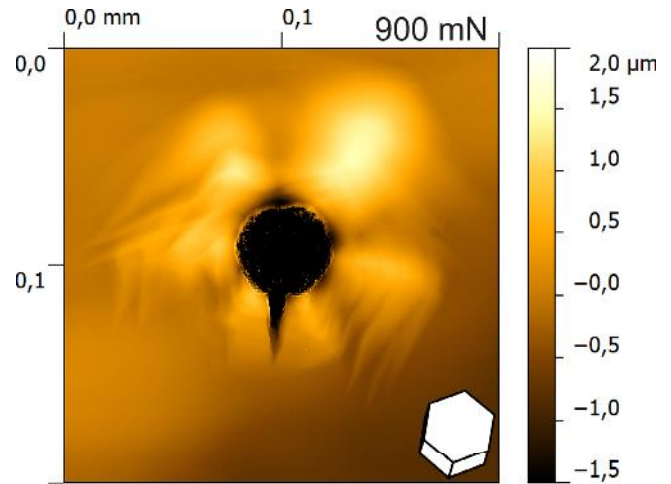**Fig. 1.** Confocal microscopy topographic image of a 90°-conical indent in pure magnesium with an indentation axis 14° away from the ⟨c⟩-axis; the maximum load was 900 mN; a crack-like feature extends from the lower side of the indent.
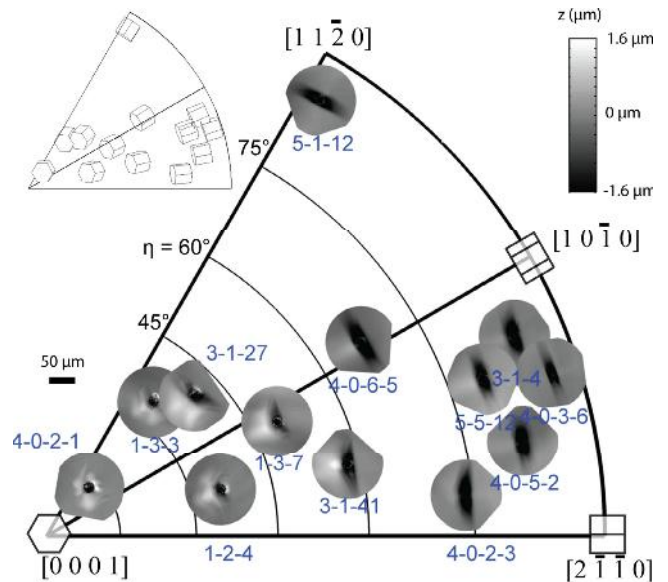

Fig. 2. Orientation dependent indent topographies for conical indentation of magnesium; inverse pole figure representation of indent topographies; maximum load 300 mN; tip radius 1 μm; orientations were in-plane rotated to follow the convention given in Ref. [75]; the inset is a visualization of the hexagonal lattice cells.

Some numerical values of the indent dimensions, maximum pile-up heights and sink-in depths are given in Table 1. For indentation axes less than 15° away from the basal great circle, little piling-up is observed. The maximum pile-up elevations were measured for indentation between 15° and 60° away from the ⟨c⟩-axis and they amounted to about 10% of the indentation depth. These pile-up elevations are formed on the "inner" side of the indents which are facing the $[0\,0\,0\,1]$-pole. They are often split into two neighboring separate pile-up maxima. Occasionally, the opposite side of the indents, away from the $[0\,0\,0\,1]$-pole, exhibits a narrowly confined and sharp protrusion right at the rim of the indent. This behavior appeared only for η-angles below 45°.

Table 1. Depth and size of conical indents with 300 mN maximum load; rows are sorted by the polar angle, η, where 0° is $\langle c \rangle$-axis indentation and 90° would be indentation along directions on the basal great circle such as $[2\bar{1}\bar{1}0]$ or $[10\bar{1}0]$. Depth values are approximate, because of reflection artifacts during confocal measurements. "Pile-up I" and "II" denote the highest and second highest surface elevation around the indent, "–" indicates that no pile-up was identified. "Sink-in" refers to the approximate lowest surface height which was not in contact with the indenter, i.e. which is part of the topography around the indent and not of the actual impression.

η (°)	Indent ID	Depth (µm)	Diameter (µm)	Pile-up I (µm)	Pile-up II (µm)	Sink-in (µm)
13	4-0-2, 1	11	25	1.0	0.8	−0.5
34	1-3-3	11	24.5	1.0	0.75	−0.8
40	3-1-27	12	25.5	1.1	1.0	−2
50	1-3-7	12	25	1.3	1.0	−1.3
58	3-1-41	12	24	1.5	–	−3
67	4-0-6,5	13	25	0.8	–	−4
74	4-0-2,3	12	22	0.2	–	−3
79	5-5-12	12	24	0.5	–	−3
87	4-0-3,6	10	22	–	–	−2.5

Toward the indentation axes on the basal great circle, groove-shaped sink-in topographies extend from both sides of the indents. Just outside the contact perimeter of the indent, these topographic features can reach depths of approximately 25% of the indentation depth, see Table 1. For these orientations, the pile-up heights are decreasing and on the basal great circle only minimal pile-up on both sides of the grooves parallel to the basal plane trace is observed. Because of the applied in-plane rotation convention, the elongated sink-in grooves are aligned with the basal great circle in the ND-IPF representation in Fig. 2. Also the edges of the sink-in grooves are parallel to the basal plane traces on the indented surface.

The orientation dependence of the maximum indentation depths showed about 20% difference between the softest and hardest crystallographic directions which is on the same level as the maximum indentation depth in grade 2 titanium [70]. In the case of magnesium, however, the hardest direction (i.e. the minimum indentation depth) was measured on the basal great circle ($\eta = 90°$) whereas in titanium the $\langle c \rangle$-axis direction showed maximum resistance.

The largest indentation depths in magnesium, on the other hand, were observed for indentation directions between 45° and 75° away from the $\langle c \rangle$-axis. Consequently, these are the softest directions of axisymmetric indentation in magnesium with a 90° conical indenter.

An additional feature of the topographies was the strongly localized pile-up that sometimes appeared at the rim of the indentations. An example is indent 3-1-41, where this type of pile-up also leads to the largest observed pile-up height of 1.5 µm for the 300 mN indentations.

3.2. Extensive glide steps from basal slip

Slip lines parallel to the basal plane trace were observed at distances from the actual indentations as large as ten times the impression diameter and beyond. The optical micrograph in Fig. 3 illustrates the large distances at which basal glide steps were present for specific orientations. In this figure the distance from the indent center to the upper right corner where the glide steps extend beyond the image dimensions is approximately eleven times the impression diameter. The glide step heights depend on the indented orientation and the strongest formation of glide steps was observed for indentation directions close to the basal great circle as shown in Fig. 3 for an indentation 5° away from
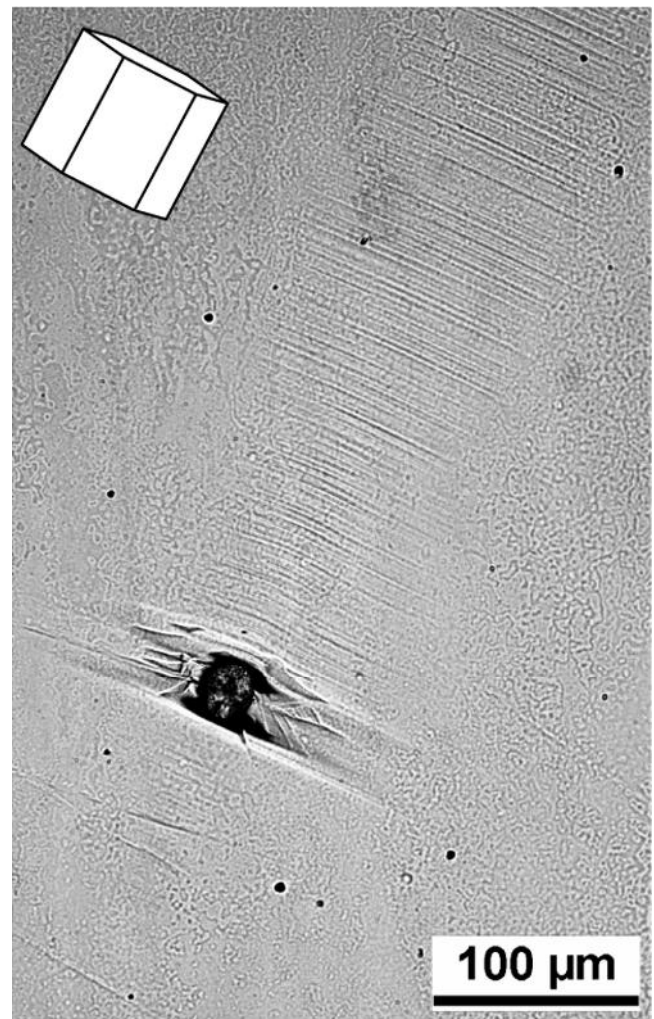

Fig. 3. Light microscopy image of indent 3-1-4, c.f. Fig. 2, $\eta \approx 85°$; the slip lines are aligned with the trace of the basal plane as determined from the EBSD-measured orientation which is visualized by the lattice cell.

the basal great circle ($\eta \approx 85°$). For these orientations basal slip traces were visible on both sides of the groove-shaped topographies, but on the "inner" side (facing the [0001]-pole in Fig. 2, upper right-hand corner in Fig. 3) they were

longer and more pronounced than on the opposing "outer" side.

3.3. Orientation dependent twinning microstructures around indentations

Fig. 4 displays representative twinning microstructures for conical indentations in four different orientations for maximum loads of 50 mN, 100 mN and 300 mN. For indentation directions close to the $\langle c \rangle$-axis, the twin stacks align with the indents in a more tangential fashion, Fig. 4a.

For indentation axes between 30° and 75° away from the $\langle c \rangle$-axis, Fig. 4b and 4c, two predominant extension twin bundles spread on the side closer to the $\langle c \rangle$-axis pole in the ND-IPF display. The indents in Fig. 4d, 3° away from the basal great circle ($\eta = 87°$), show profuse twinning that is mostly confined inside the grooves from the topographical measurements.
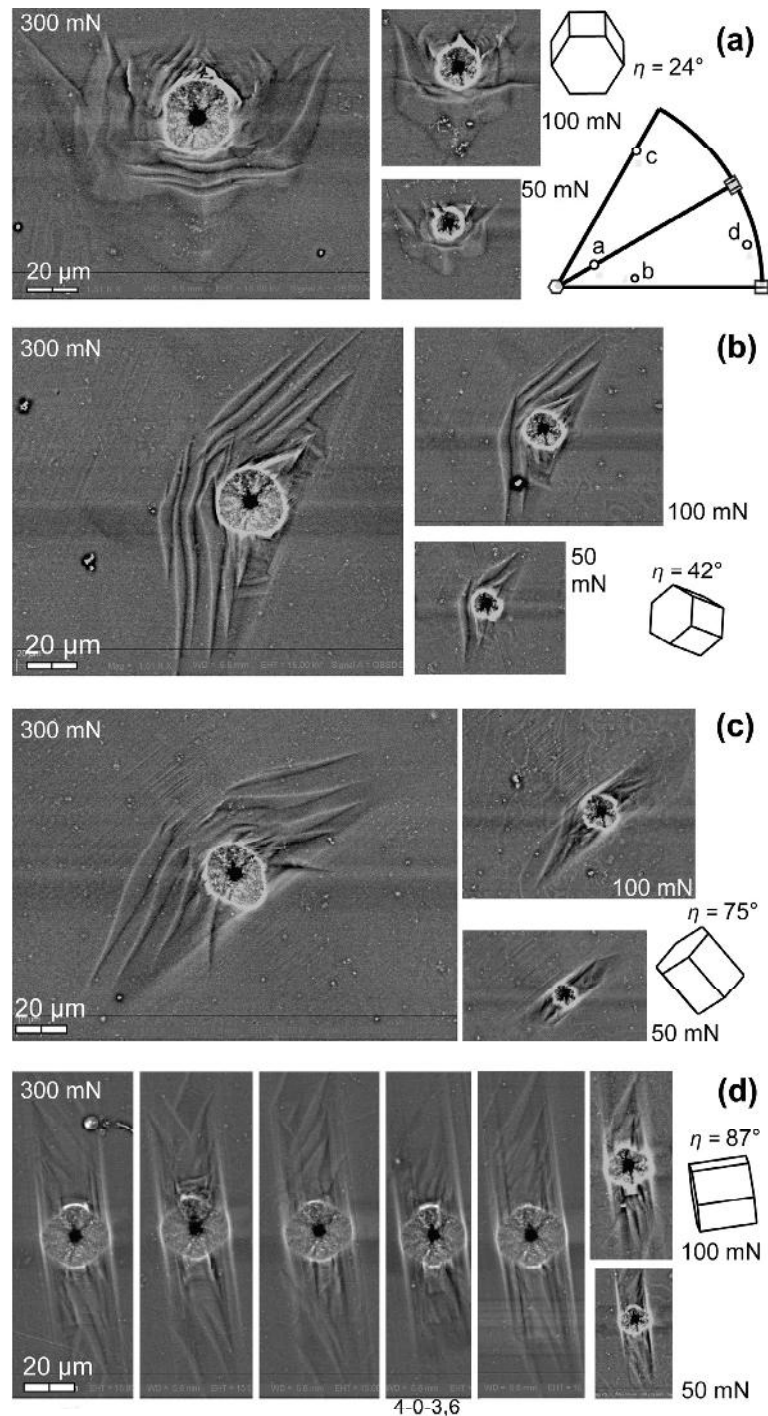

Fig. 4. Conical indentation of magnesium; backscatter electron images of representative indents with maximum loads of 50, 100 and 300 mN, (a) indentation direction 24° away from the $\langle c \rangle$-axis, 4-0-(2,12) (300 mN); (b) 42° from the $\langle c \rangle$-axis, indent 4-0-(2,10) (300 mN); (c) 75° from the $\langle c \rangle$-axis, 4-0-(2,4) (300 mN); (d) 87° from the $\langle c \rangle$-axis, e.g. 4-0-(3,6) (300 mN).
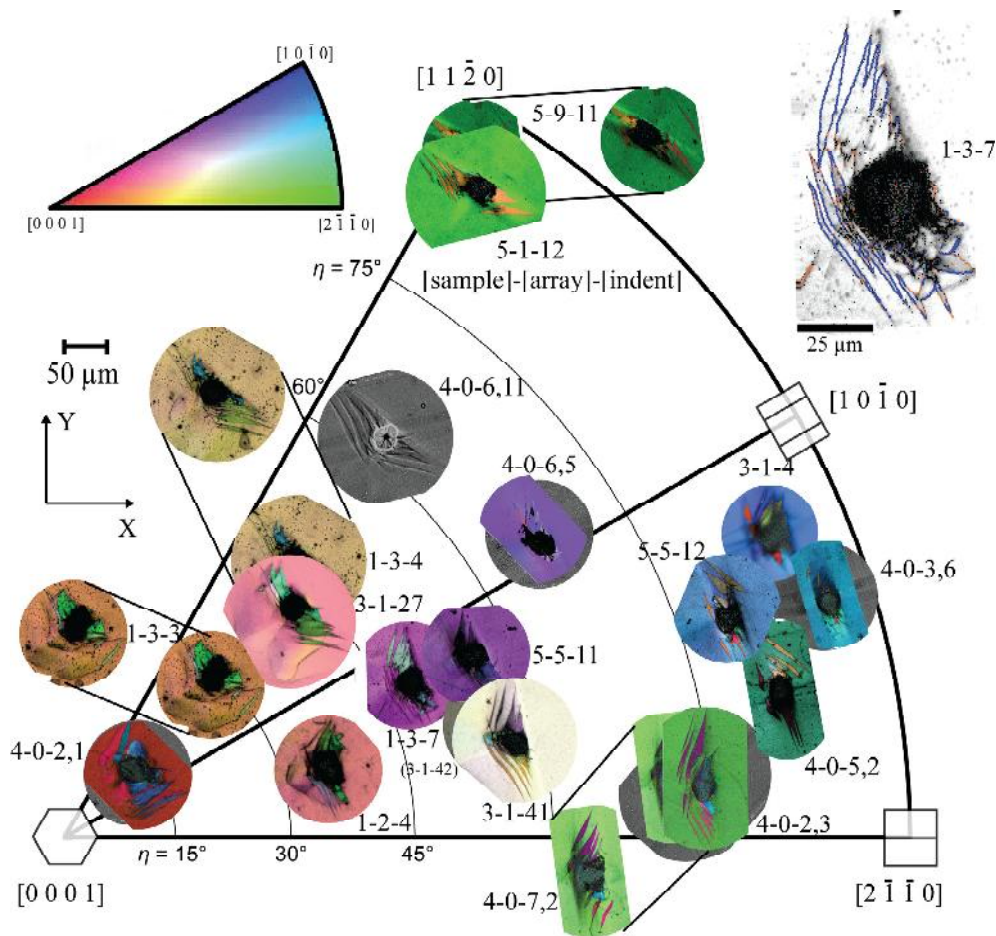
Fig. 5. Inverse pole figure (ND-IPF) of indent microstructures after 90° conical indentation in pure magnesium; maximum load 300 mN; the indent microstructures are represented by EBSD orientation maps colored by the ND-IPF color scheme. Also shown is one instance of a backscatter electron image of indent 4-0-(6,11). The inset on the upper right side illustrates the extension twin boundaries of indent 1-3-7, as identified by their misorientation and plane trace (blue: plane trace tolerance 1.5°, orange: above 1.5° plane trace deviation). (For interpretation of the references to color in this figure legend, the reader is referred to the web version of this article.)

To analyze the crystallographic relations of the twinning microstructures around indents in more detail, orientation maps of individual indents were acquired at higher resolution (step size 0.5 μm). Again, these maps were rotated according to the same in-plane orientation convention as used for the indent topographies. The resulting ND-IPF of the indent microstructures is given in Fig. 5. Due to the color contrast in the orientation maps, the orientation dependence of the twinning microstructures can be readily analyzed in this figure. In the EBSD orientation maps, twinning around the indents can be reliably discriminated even in cases that do not produce strong contrast in BSE imaging. Analysis of the EBSD data revealed that only extension twinning on $\{10\bar{1}2\}$ planes was observed at the surface.

To confirm the 3D nature of the observed twinning microstructures, electrolytic polishing after indentation was applied on sample number 3 and afterward additional orientation mapping was performed. Fig. 6 shows an example of the resulting EBSD ND-IPF maps that were collected in this way. The orientation maps that were acquired below the original sample surface clearly showed that the twin ledges extend well below the sample surface. The twins also were observed to have a larger width inside the sample than at the surface.

3.4. Activated twinning variants depending on the indented orientation

For all orientations certain subsets of the available twin systems were visible at the surface. There are six extension twinning systems, one for each of the six $\{10\bar{1}2\}$ planes, Table A.3.

Depending on the twin width, the long axis of the twins and on the surface topographies, the twinned regions were indexed with different reliability during EBSD measurements. Thin twin ledges were sometimes indexed as the parent orientation and could only be revealed by the variation of the Kikuchi pattern quality measure along their boundaries in the EBSD data or by orientation contrast in the backscatter imaging.

Identification of individual twin systems was performed based on a combined analysis of crystallographic misorientations and the alignment between the twin boundaries and the twin plane traces. First, the average orientations of the indented grain and each twin type visible in the EBSD data were extracted. Then the misorientation between each of these experimental orientations and each of the theoretically expected twin orientations (a 180° rotation about the $\langle 10\bar{1}1 \rangle$ axes of the indented grain) was calculated, see Fig. 7 and Table 2. All experimental twin
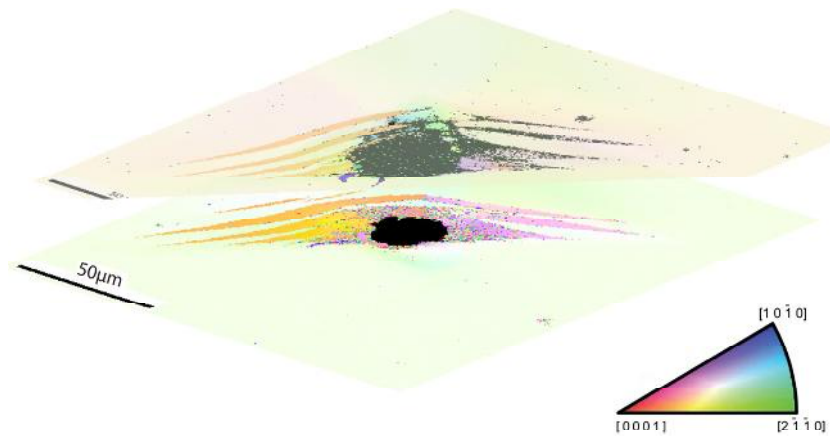
Fig. 6. Serial polishing in combination with EBSD confirmed the three-dimensional nature of the observed twinning patterns; indent 3-1-41, 58° from the $\langle c \rangle$-axis; the second map was collected approximately 5 μm below the initial surface measurement (estimated height difference based on the difference in indent sizes and the known indenter geometry); the IPF color legend refers to the indentation direction. (For interpretation of the references to color in this figure legend, the reader is referred to the web version of this article.)

Table A.3. Labels of the extension twinning systems as used in the text.

No.	Twin direction	Twin plane
T1	$[\bar{1}011]$	$(10\bar{1}2)$
T2	$[0\bar{1}11]$	$(01\bar{1}2)$
T3	$[1\bar{1}01]$	$(\bar{1}102)$
T4	$[10\bar{1}1]$	$(\bar{1}012)$
T5	$[01\bar{1}1]$	$(0\bar{1}12)$
T6	$[\bar{1}101]$	$(1\bar{1}02)$

orientations showed a small misorientation from one or more expected twin orientations. For several twin stacks, the misorientation from the expected twin orientations could not identify the twinning variant uniquely because two possible twin variants were found within a misorientation range of up to 10°. In those cases it was often possible to identify the twin variant by comparing the twin boundaries with the $\{10\bar{1}2\}$ plane trace. This trace analysis argument is illustrated in Fig. 7 and referred to in Table 2. For some of the smaller twin packets, no alignment with an expected surface trace could be reliably identified and no final decision was made regarding the twinning system.

A minimum number of two twin variants were observed throughout the experimental data for all indented orientations. Due to ambiguity in some of the identified twin systems, the maximum number of variants observed at the surface of a single indent is either three or four.

Further analysis of the identified twinning systems revealed a characteristic behavior of the observed twinning modes. Generally, for indentation axes in the intermediate range of polar angle, η, the twinning shear directions followed a specific sense. For these indentations, the twin laths extended along a roughly tangential direction of the circumference of the indent. The twin shear sense on the outer side of the twin, away from the indent center and usually toward the $[0001]$-pole in the IPF representation, was often found to point upward, out of the sample surface. On the side closer to the indent center the out-of plane component of the twinning shear was then pointing into the sample. However, these observations might depend on the magnitude of the out-of-plane component of the twinning shear.

3.5. Confined lattice rotation zones

One microstructural feature which was observed for indentation directions of low and intermediate values of angle η of about 15–45° from the $\langle c \rangle$-axis, were confined rotation zones. These regions exhibited lattice rotations of up to around 10° from the orientation of the indented grain. Fig. 8 shows an example of such a rotation zone colored by the lattice rotation with respect to the average parent grain orientation. Shown in Fig. 8c is another instance of localized lattice rotation, observed in indent 3-1-41.

3.6. Twin statistics from backscatter electron imaging

Different orientations exhibited distinct twinning behavior. Some orientations showed highly reproducible twinning characteristics whereas for others significant scatter was present regarding the number of twin laths and the activated twin variants. The indented grains in sample four showed a wide spread of crystallographic indentation directions. Therefore, extensive BSE imaging on this sample was performed to investigate the statistical nature of the twinning microstructures that developed around the indents.

The individual twin areas were measured by manually highlighting the twin ledges in a commercial image processing software, Fig. 9a. Alternatively, for good imaging conditions during EBSD measurements, which resulted in reliable indexing of the thin twin laths, the twin areas could be directly extracted from the mapped orientation data. The cumulative twinned area was easily two to over three times as large as the projected area of the impression for many indents.

For example, in the case of indent 3-1-41 the indent diameter was around 24 μm and the predominant twin system (twin stack "B" in Fig. 7b) formed four twin lamellae with areas 252 μm², 267 μm², 185 μm² and 124 μm², as extracted from EBSD data. This results in an area ratio of about 1.8 for twinned area over indent area just for the prevalent twinning system.

Due to frequent incorrect indexing of the second most visible twin type, the area ratio between the first and second most visible twin system can only be estimated to be

approximately 1:1, which yields an area ratio between the twinned area and the impression of about 3.7.

Some values for the normalized twin area (NTA),

$$\text{NTA} = \frac{\sum_i A_{\text{T}_i}}{A_{\text{ind}}} \tag{1}$$

between the total twinned area, A_{twin}, and the projected area of the remaining impression, A_{ind}, are given in Fig. 9b. The indent areas were calculated by assuming a circular shape of the indent.

The largest total twin areas were observed for indents 3-1-41 and 4-0-(7,9), see Fig. 9a. The side of the indent 4-0-(7,9) facing the [0 0 0 1] pole (along the direction of the $\langle c \rangle$-axis out of the sample surface, to the upper right corner in Fig. 9a) exhibits two twin bundles. For indents in the same grain these bundles sometimes intersect besides the indent and commonly one of the bundles is prevalent. For these indents, the total twinned area was more than three times as large as the projected area of the impression. For this indentation direction, together with indent 3-1-41, also the highest number and longest extension of well
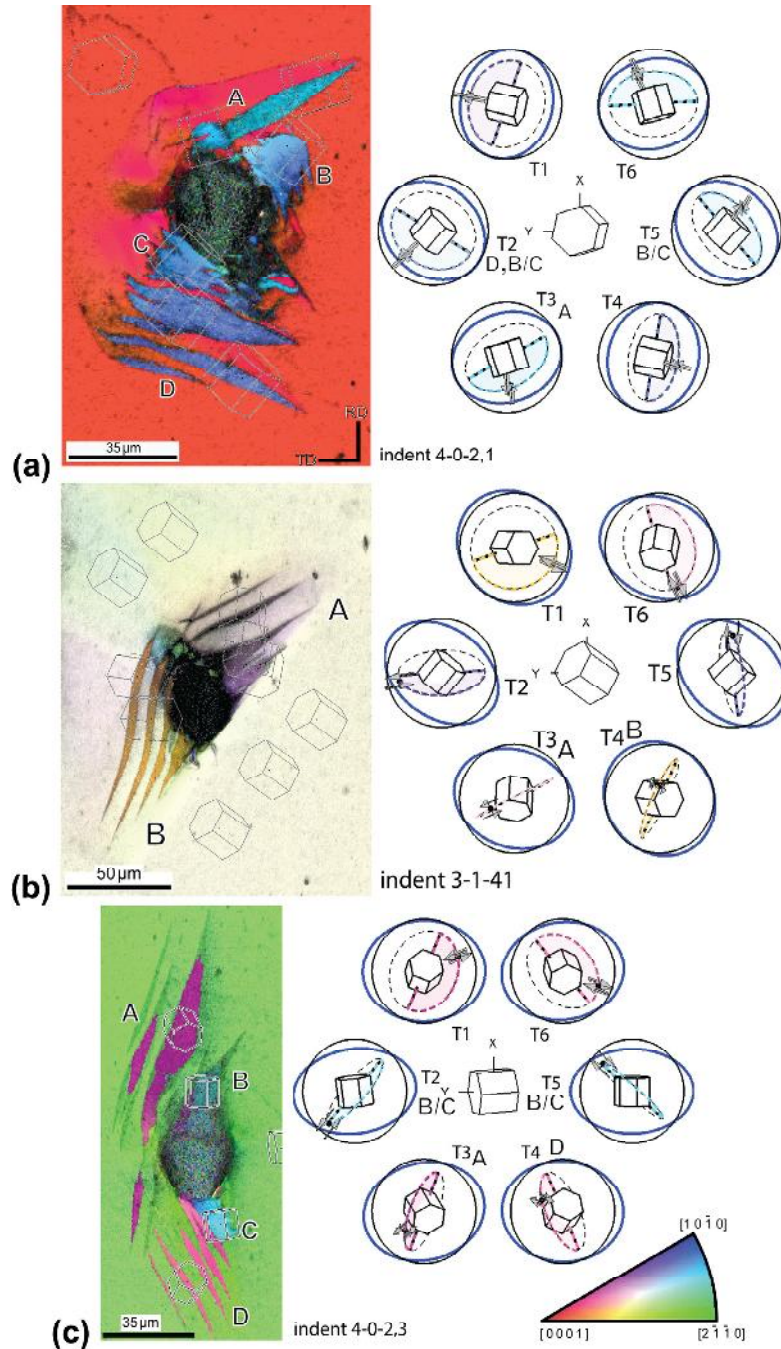

Fig. 7. EBSD orientation maps (ND-IPF coloring) of indents in magnesium; the lattice cells outside the EBSD map represent the six theoretical twin variants that are expected based on the parent grain orientation; their twin planes and traces are illustrated along with the twinning shear directions. Additionally, the twinning strain in the indented plane is visualized by strain ellipses (amplified by factor 3); (a) indent 4-0-(2,1) 13° from $\langle c \rangle$-axis; (b) indent 3-1-41, 57° from $\langle c \rangle$-axis; (c) indent 4-0-(2,3), 74° from $\langle c \rangle$-axis.

Table 2. Crystallographic misorientations between the experimentally measured twin orientations (Exp. A, B, …) from Fig. 7 and the expected twin orientations calculated from the parent grain orientations (T1–T6). The experimental twin variants were identified based on low misorientation and their boundaries' alignment with the twin plane trace; coloring is according to the ND-IPF color scheme from Fig. 7.

Ind. 4-0-2 1

	T1	T2	T3	T4	T5	T6	Aligned with trace / identified as
Exp.A			0.9			6.5	T3
Exp.B	-	5.2	-	-	2.6	-	T2/T5
Exp.C	-	4.4	-	-	3.6	-	T2/T5
Exp.D	-	1.4	-	-	7.9	-	T2

Ind. 3-1-41

	T1	T2	T3	T4	T5	T6	Aligned with trace / identified as
Exp.A	-	-	4.6	-	-	6.7	T3
Exp.B	7.2	-	-	1.4	-	-	T4

Ind. 4-0-2 3

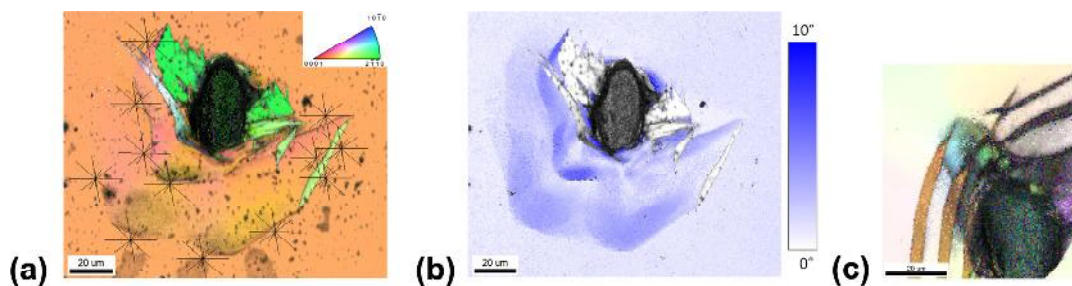|	T1	T2	T3	T4	T5	T6	Aligned with trace / identified as
Exp.A	-	-	1.7	-	-	6.3	T3
Exp.B	-	6.4	-	-	4.9	-	T2/T5
Exp.C	-	5.6	-	-	4.4	-	T2/T5
Exp.D	-	-	-	2.6	-	-	T4

Fig. 8. Indent in high purity magnesium (a, b: indent 1-3-3, indentation direction 34° away from the $\langle c \rangle$-axis); (a) ND-IPF coloring combined with a grayscale map of the EBSD pattern quality, plane traces are for extension twinning systems; (b) lattice rotation (0…10°) away from the orientation of the undeformed region; twins are white, but have a misorientation larger than 10°; (c) magnified view of the localized pile-up of indent 3-1-41, which also shows lattice rotation of up to 15°, indicated by the bluish/green ND-IPF coloring. (For interpretation of the references to color in this figure legend, the reader is referred to the web version of this article.)

developed twin laths were found at the sample surface. In the IPF representation, a sharp edge of basal slip activity is found on the "outer" side of the indent, facing the basal great circle (in the lateral direction corresponding to moving along the $\langle c \rangle$-axis into the sample). No steep topography from the basal slip is found on the "inner" side (facing the $\langle c \rangle$-axis pole in the IPF representation) of the impression where the deformation seems to be realized primarily by twinning.

4. Crystal plasticity finite element simulation of indentation in magnesium

4.1. Geometrical setup of the model

To support the analysis of the observed twin microstructures, three-dimensional crystal plasticity finite element simulations of the indentation process were performed. This kind of modeling has been applied frequently to simulate the deformation during indentation of single crystals [76–80,75,81,70]. For deformation by a sharp conical tip as used in the experiments, the discretization into finite elements is challenging. Since the load is highly concentrated at the tip of the indenter, the elements in the center of the

finite element mesh get highly distorted. Therefore the simulations employed a tip with a larger radius to alleviate the stress concentration under the tip. The nominal tip radius of the indenter in the experiments was 1 μm. In the simulations a sphero-conical tip with a radius of 4 μm was modeled, leading to a truncation difference of $\Delta h_{4\mu m} - \Delta h_{1\mu m} = 1.24\ \mu m$. The maximum indentation depth prescribed in the model was 12 μm. The indenter was represented by a rigid surface with a tangential continuation of the spherical part into the conical part.

Fig. 10 depicts the deformed finite element mesh after crystal plasticity simulation of sphero-conical indentation in magnesium. The model was generated parametrically in the preprocessor software *MSC Mentat* by a set of *Python* routines [82] which were used to generate *Mentat procedure* files. The model was set up with displacement controlled movement of the indenter to arrive at the maximum indentation depth after ten seconds.

4.2. Modeled deformation systems

The constitutive law that was used in the simulations is an elasto-viscoplastic phenomenological crystal plasticity model [83,80]. The specific implementation applied here is described in more detail elsewhere [75,70]. It is a
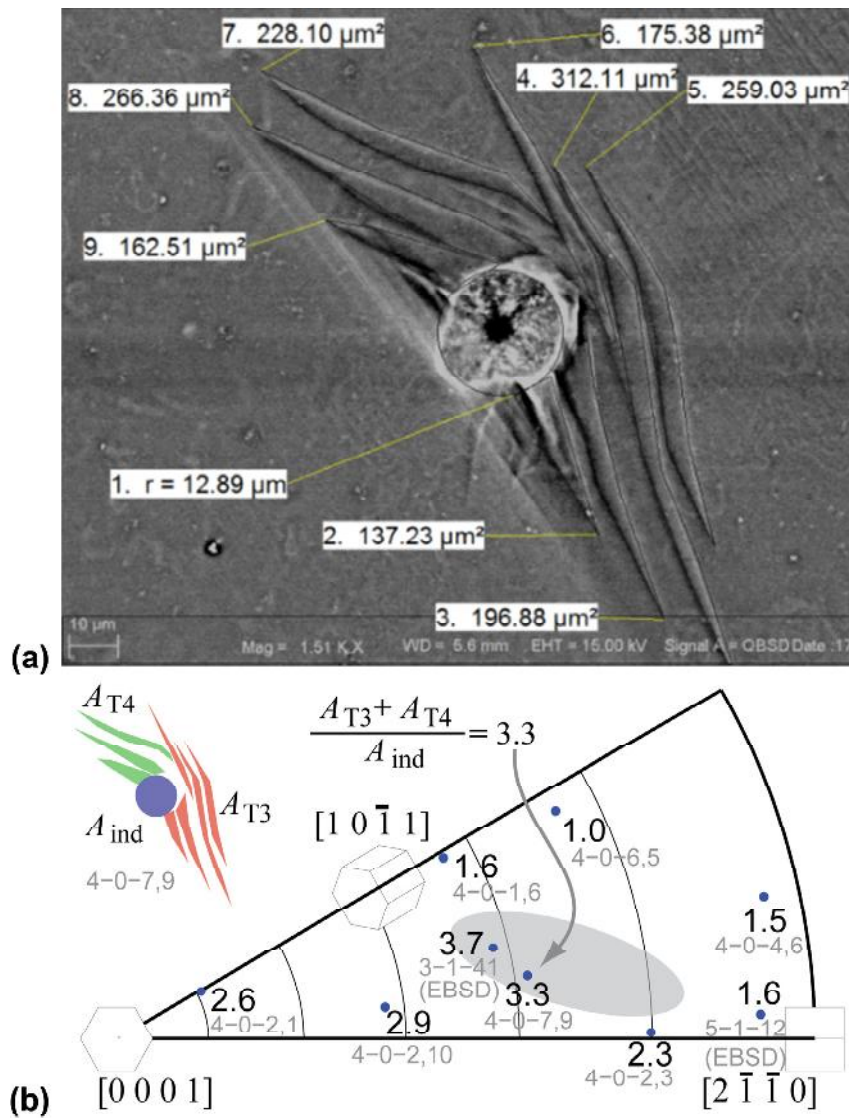
Fig. 9. (a) Determination of twin area and impression diameter for indent 4-0-(7,9); (b) inverse pole figure of indentation axes in single crystal magnesium; the shaded region outlines the orientations for which the twinning microstructures with the longest twin laths and largest total twinned areas were identified; also given are some numerical values of the normalized twin area (NTA), the ratio between the cumulative twinned area, A_{twin}, and indent size, A_{ind}.

predecessor of the *DAMASK* [84,85] code base and employs a user-defined material subroutine to interface the constitutive law with the finite element solver, here the *hypela2* subroutine of the finite element solver *MSC Marc*.

For the 3D crystal plasticity simulation of conical indentation in magnesium the following deformation mechanisms were taken into account: three basal slip systems of type $\{0001\}\langle11\bar{2}0\rangle$ and six extension twinning systems of type $\{10\bar{1}2\}\langle10\bar{1}1\rangle$.

The twinning systems were not modeled based on a volume-fraction per twinning system with a fixed twin shear [86] but were assumed as unidirectional slip modes, exactly as given in Zambaldi and Raabe [75]. A continuous distribution of shear values resulted from this simplification.

Prismatic $\langle a\rangle$-glide was not included in the simulations since Chapuis and Driver [40] found it to contribute to the plastic deformation significantly only at temperatures above 300 °C. The experimentally observed indent

topographies and slip lines did also not show any evidence of this deformation mode. Dislocation slip systems with a shear component along the $\langle c\rangle$-axis, such as pyramidal $\langle c+a\rangle$-slip, were also neglected.

4.3. Simulation parameters

The anisotropic elasticity of magnesium was taken into account and the elastic constants $c_{11} = 58.0$ GPa, $c_8 = 25.8$ GPa, $c_{13} = 20.8$ GPa, $c_{33} = 61.2$ GPa, $c_{44} = 16.6$ GPa and $c_{66} = 16.5$ GPa were used [87]. To facilitate the comparative analysis between slip and twinning the same constitutive parameters were assigned to slip and twinning systems. An initial shear strength, τ_0, of 10 MPa, a saturation shear strength, τ_s, of 100 MPa, an initial hardening slope parameter, h_0, of 100 MPa, and a saturation hardening exponent, a, of 2.0, were used for all simulations, c.f. [75] for details about the constitutive law. The reference shear rate was $10^{-3}\,s^{-1}$ and the latent hardening coefficients between all
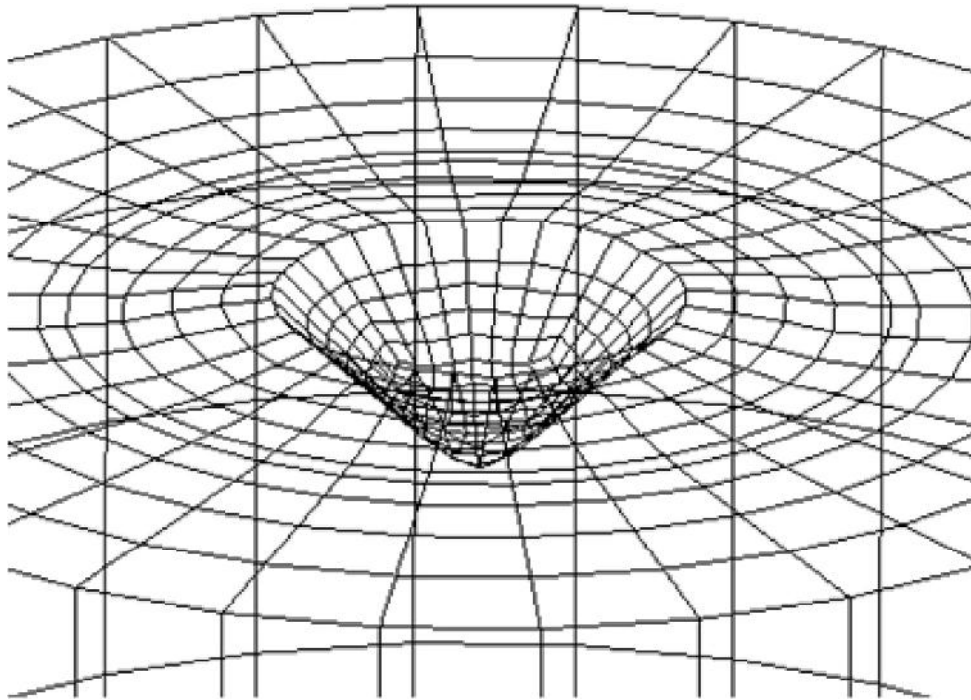
Fig. 10. Deformed finite element mesh of a crystal plasticity simulation of conical indentation in magnesium; $\langle c \rangle$-axis indentation; 4320 linear eight-node brick elements were used.

deformation systems were arbitrarily set to 0.2. The exponent of the viscoplastic law was 20.

4.4. Simulation results

For the analysis of the shear contributions from each deformation system, the CPFEM results were converted into the *visualization toolkit* (VTK) file format and visualized with the software *Paraview* [88]. Due to convergence problems in some orientations and at the later stages of deformation, the results in Fig. 11 were exported at increment 400 out of 800 linearly spaced increments of the indenter position. Thus the simulated indentation depth in the results given below corresponds to an experimental indentation depth of about 7 μm. However, the main features of the simulation results such as the spatial distribution of slip and twinning activity, are not sensitive to the absolute size of the model and can therefore be discussed also at this smaller simulated indentation depth.

Fig. 11 presents the shear distribution of the active systems around a simulated indentation. Generally, lobes of slip activity are observed around single crystal indentations [75]. In the case of twinning as it was implemented in the present work the morphology of these shear zones is similar to the zones for dislocation glide. A smooth transition from zero total shear on a twin system to shear values even higher than the theoretical twinning shear is predicted by the constitutive model. No quantization of the twinning deformation into separate twin laths can be realized by the employed model.

The sharp topographic features resulting from basal slip for indents away from the $\langle c \rangle$-axis could not be reproduced by the simulations. In order to represent this kind of highly localized slip a much finer discretization of the volume would be necessary which is currently prohibitive in terms of computational cost.

5. Discussion

5.1. Ductility of polycrystalline magnesium and $\langle c + a \rangle$-slip

The (CRSS) for basal slip in pure magnesium is of the order of 1 MPa [45]. Because of its strong plastic anisotropy, pure polycrystalline magnesium presumably gains its resistance against plastic deformation primarily from effects that act in addition to the intrinsic (CRSS) values of the single-crystal. For magnesium it is expected that the incompatibility of deformation between grains of different orientations and the mechanical barrier effect of grain boundaries should be of importance. To understand the relative contributions from these effects, it is necessary to isolate and identify the underlying single crystalline mechanics. Only then can the additional effects on the micromechanical behavior of polycrystalline material be quantified.

Since strong plastic anisotropy of the grains in an aggregate leads to stress concentrations during deformation, e.g. [89], and in the case of magnesium to early fracture initiation and low room temperature ductility, the activation of non-basal deformation systems other than twinning is desirable. Indentation testing imposes a three-dimensional deformation which cannot be accommodated only by slip on the basal plane. Therefore, it seems to be of value in assessing the activation of non-basal deformation systems. Here, in the case of pure magnesium, because of the dramatic increase in the resolved shear stresses necessary to activate either basal slip and extension twinning or the
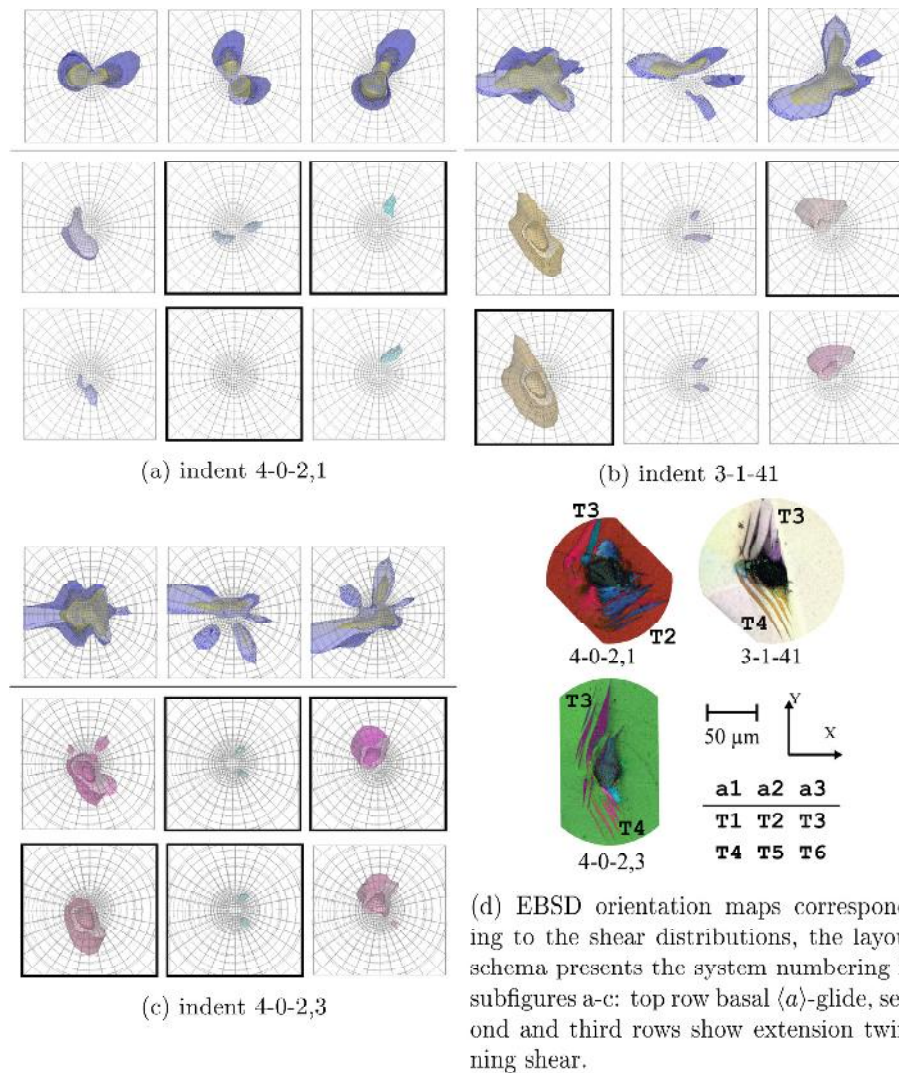
(a) indent 4-0-2,1

(b) indent 3-1-41

(c) indent 4-0-2,3

(d) EBSD orientation maps corresponding to the shear distributions, the layout schema presents the system numbering in subfigures a-c: top row basal $\langle a \rangle$-glide, second and third rows show extension twinning shear.

Fig. 11. Top views on the 3D spatial distribution of shear on different deformation mechanisms as predicted by crystal plasticity simulation of sphero-conical indentation in magnesium; isosurfaces for specific shear values are shown. Subfigures (a–c) show top views on simulation results for indentation in crystals with orientations from the IPF representation, Fig. 5 and reproduced in subfigure (d). Each view includes an area of 60 μm × 60 μm. Blue and yellow colors denote basal slip in directions a1, a2 and a3 at shear values 0.06 (blue) and 0.13 (yellow). The isosurfaces of the twinning shear are colored based on the corresponding IPF coloring of the respective twinning variants. For the pseudo-twinning systems the isosurfaces are drawn in identical colors at shear levels 0.02 and 0.13. The arrangement of the shear maps is chosen such that two twin systems which are shearing in the same plane (T1/T4, T2/T5, T3/T6) are vertically aligned, see legend in subfigure (d). Framed twin variants were identified in the experiments, c.f. Fig. 7 and Table 2. (For interpretation of the references to color in this figure legend, the reader is referred to the web version of this article.)

other possible deformation mechanisms, no direct and unambiguous evidence of $\langle c + a \rangle$-slip was found.

5.2. Discussion of basal glide steps

Basal $\langle a \rangle$-glide is the deformation mechanism which is easiest to activate in magnesium. However, even for the minimal CRSS values of basal $\langle a \rangle$-glide, the distances for which basal slip activity was directly observed by slip lines, are intriguing.

Basal slip traces were most pronounced for indentation directions that are closer to the basal great circle. For these orientations, the imposed deformation cannot be easily accommodated by basal slip alone because the $\langle a \rangle$-glide systems shear on a plane which is almost perpendicular to the sample surface. Therefore, they cannot efficiently realize

compressive deformation along the direction perpendicular to the basal plane trace. Because of this difficulty to accommodate the indentation deformation, long-range compressive stress fields remain on both sides of the groove-shaped topographies in the directions perpendicular to the groove's longitudinal axis, Fig. 12. Accordingly, the significant basal slip activity far from the actual indent position is a direct consequence of the strong plastic anisotropy of magnesium.

5.3. Discussion of the orientation dependent topographies

Regarding the general orientation dependence of the indent topographies, similar orientations showed comparable patterns. The polar angle, η, was found to be the primary influence on the morphology of the indentations.
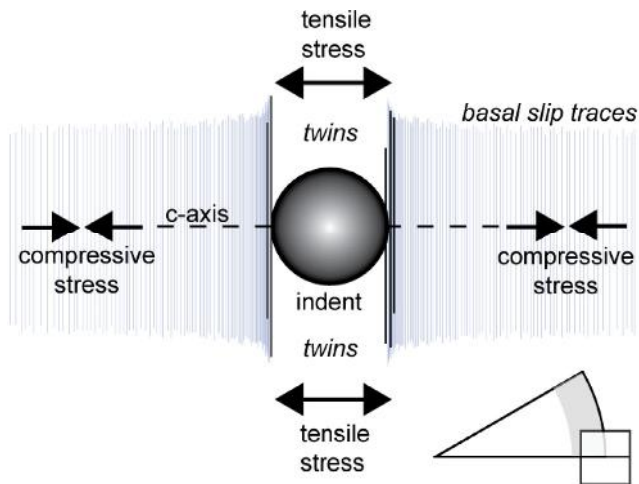
Fig. 12. Schematic illustration of the micromechanical situation during indentation of magnesium perpendicular to the $\langle c \rangle$-axis.

Even with the added complexity of twinning deformation, the relative activation of slip and twinning modes seems to largely follow a smooth function in orientation space. Therefore, it should be possible to interpolate between results from sufficiently similar orientations.

For indentation of magnesium, the observed pile-up topographies are not as prominent as in titanium [70]. In titanium the pronounced pile-up of material along the $\langle a \rangle$-slip directions for indentation axes not parallel to the $\langle c \rangle$-axis is directly related to the primary activation of prismatic $\langle a \rangle$-glide. In magnesium, for the same orientations, glide steps and some localized sink-in is observed and can be linked to the activation of basal $\langle a \rangle$-glide.

For indentation close to the $\langle c \rangle$-axis, however, titanium shows almost no pile-up of material, whereas magnesium displays significant upheaval. The sources of this change in the topography could be subsurface twinning, $\langle a \rangle$ or $\langle c + a \rangle$ dislocation glide. No clear traces of $\langle c + a \rangle$-slip were identified. The topographies for indentation close to the $\langle c \rangle$-axis indicate some pile-up from subsurface twinning mixed with pile-up from basal $\langle a \rangle$-glide. The analysis is complicated by the concurrent activation of different kinds of deformation systems and potential interactions between those. Thus the topographies that develop during indentation of magnesium along and close to the $\langle c \rangle$-axis are currently evading a comprehensive analysis. Selvarajou et al. [74] performed an in-depth analysis of the pile-up profiles during $\langle c \rangle$-axis-indentation to different indentation depths.

The data given in Table 1 show that sink-in is the dominant phenomenon in comparison to the pile-up for most orientations. Because of that we will focus in the following on the sink-in patterns that develop for indentation axes close to the basal great circle. The groove-shaped topographies that were found for indentation away from the $\langle c \rangle$-axis could in principle be explained by at least two different mechanisms: first by basal slip activity, since their edges are aligned with the traces of the basal planes, second they could also form as a result of pronounced twinning close to the indenter. Both possibilities are discussed in the following.

Twinning around the indents introduces new densely spaced interfaces which can act as dislocation [90] and twin [54,36] barriers. The increasing number of boundaries leads

to progressive hardening of the material around the indent. High levels of strain hardening are known to lead to sink-in of the material around indentations [91,92,79]. This ad hoc explanation of the local mechanics seems to be supported by the sink-in grooves that were observed for indentation axes in or close to the basal plane, where intense twin activity was present inside the sunk-in regions. However, the groove-like topographies were also observed in the 3D modeling which does not properly take into account the hardening effect of the twin interfaces. This discrepancy hints to the alternative explanation of the sink-in by basal slip. It is also promoted by literature data on indentation of other materials: the significance of basal $\langle a \rangle$-dislocation glide for the formation of the elongated grooves could be deduced from comparisons to the impression shapes of ZnO [68] or beryllium [65]. Their respective indent topographies show similar grooving with no (ZnO) or little (Be) surface connected twinning. Corresponding half-loop configurations of dislocations have been observed by Hockey [93] and later discussed by Basu and Barsoum [68] for zinc oxide. The absence of twinning in these cases enables a selective verification of the effects of basal slip activity on the resulting indent topographies. This comparison supports the hypothesis, that the formation of the characteristic grooves is to large extent due to the easy activation of basal $\langle a \rangle$-glide.

5.4. Discussion of the lattice rotation zones

An often observed characteristic of the conical indentations were the lattice rotation zones in the untwinned regions around the impressions, see Fig. 8.

The analysis of activated twin modes during indentation suggests that the confined lattice rotation zones, the orientation dependence of the pile-up topographies, as well as the twinning phenomena can be jointly discussed. The sense of shear for the predominant twin systems in the intermediate orientations was found to most often have a shear direction out of the sample surface on the side away from the indent. And on the side of the twin closer to the indent, the shear sense was mostly pointing into the volume of the sample. The twinning shear sense is indicated in Fig. 7 by arrows. Based on this observation, the rotation zones could possibly be interpreted as bending or kinking of the untwinned material to accommodate subsurface or surface connected twin activity closer to the indent, Fig. 13. This kinking mechanism has been reported in the literature [94–96].
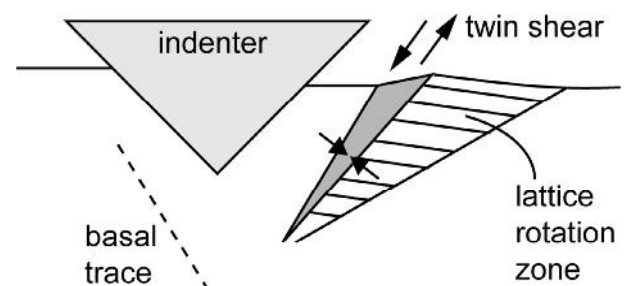

Fig. 13. Schematic of the observed lattice rotation zones; accommodation of the growing twin in the lattice rotation zone could be explained by kinking or basal slip or a combination of both.

An alternative explanation for the observed sharp interfaces was brought forward by Poole et al. [97] who speculated that the interfaces are left behind as detwinning occurs during unloading. This could well explain the sharp orientation change across the interface, because any dislocation plasticity and corresponding lattice rotations would have likely been stopped at the twin interface.

Also Shin et al. [72] observed the formation of stacking faults on the basal plane during indentation. It is possible that the formation of densely spaced stacking faults confines dislocation plasticity within the zones for which significant lattice rotations were measured.

Due to the highly heterogeneous stress fields around indentations it is possible that a combination of the mechanisms mentioned above leads to different origins of the rotation zones for various indentation axes. The structure of the lattice rotation zones could be revealed by 3D-EBSD measurements [77,71] or by targeted preparation of TEM lamellae from the rotation zones [72]. Also, in situ diffraction experiments with high-energy x-rays could probably clarify the possibility of detwinning during unloading.

5.5. Discussion of the twin microstructures around indents in single crystal magnesium

For indentation of pure magnesium the twin stacks that form around the impression are the most prominent features which can be readily observed at the surface. The microstructures around the indentations were found to be highly orientation dependent and the indentation response of the crystal is clearly connected to the underlying lattice structure. The morphology of the twins was characterized by the topographic measurements as well as by backscatter imaging. The twinning process was confirmed by EBSD orientation mapping to be of the common $\{10\bar{1}2\}$ extension twinning type. The surface twins also showed some statistical variations in terms of length and number of twin laths.

To investigate the evolution and the size-dependence of the deformation by indentation, experiments with different maximum loads were performed inside several grains, see Fig. 4. These experiments revealed that the twinning patterns after indentation with different loads share similar features. No indent was observed in situ during the indentation process. Nevertheless, because of the similar microstructures for a certain orientation, a number of conclusions can be drawn from comparing the indents performed with different loads. With increasing maximum load, the length and number of twin laths increase correspondingly, especially for indentation away from the $\langle c \rangle$-axis. In contrast, the distance between the long axis of each of the twin laths in one twin stack (a set of parallel twins) seems to stay constant. For intermediate η-values, the width of each individual twin does not seem to grow significantly with progressing deformation, while for indentation close to the $\langle c \rangle$-axis the pattern seems to grow in a more self-similar fashion.

Indentation for η-angles between about 30° and 75° lead to the most well-defined twin stacks. The individual twin laths cut the sample surface in a specific angle depending on their twin plane. This is for example illustrated by indent 1-3-7, almost in the center of the IPF Fig. 5 and also shown there as an inset twin boundary map. For this indent, the extension twinning direction $[10\bar{1}1]$ of twin system number

four (c.f. Table A.3) is almost parallel to the indentation axis with a deviation of only 3.7°. The twin plane is almost perpendicular to the sample surface in this case. This leads to the twinned area having almost the same crystallographic normal and thus a very similar color as the matrix in the ND-IPF orientation map. Due to this unique configuration, the observed twins of this system (T4) run tangential and almost symmetrical to the edge of the indent and also parallel to the basal slip traces. The twin laths also appear thinner in comparison to other systems, because they are cut edge on. The observation of twins parallel to the basal plane trace corresponds directly to the twinning microstructures that were reported for indentation along $[1\bar{1}00]$ where most twin laths run parallel to the basal plane trace in the same fashion [73, Fig. 3a].

Examples of the area ratio of total twinned area, as quantified on the surface by EBSD or SEM, to the indent area were given in the results section, see Fig. 9. Other measures of twinning activity could be developed. For example the cumulative area or length of twins could be separately analyzed by twin variant.

The crystallographic orientations in the upper and lower half of the ND-IPF representation are connected through an improper symmetry transformation. Accordingly, the microstructures around indents in two orientations that are related in this way will exhibit mirror symmetry [75]. This mirror symmetry is observed in the microstructures of indents 3-1-41 and 4-0-(6,11) in Fig. 5. If these two orientations are reduced to the smaller fundamental zone by allowing for improper transformations, their indentation axes deviate by only 5° from each other. Their indent microstructures are an almost perfect mirror image of each other.

The statistical variance of the indent patterns and the derived measures is expected to follow a specific orientation dependency. For indentation directions close to planes of symmetry the statistical variance should be increasing since symmetric twin variants are similarly easy to activate in this case. This behavior was for example found for indents in the same grain as indent 4-3-6, with an indentation axis just 3° from the basal great circle, Fig. 5: trace analysis in seven BSE images revealed that inside the grooves, the twin bundles on both sides of the indentations were selected from complementary types (T3/T6, T1/T4) in a rather random fashion.

On the other hand, indentation directions which show pronounced twinning but at the same time exhibit low statistical variance exist, e.g. for an η-angle of around 60° for orientations approximately between indent 3-1-41 and indent 4-0-(2,3). These orientations can also be described in the ND-IPF as lying inside an elongated region between indentation parallel to the twin shear direction $[10\bar{1}1]$ and $[2\bar{1}\bar{1}0]$, see the shaded region in Fig. 9. Due to the clearly discernible twin lamellae, the amount of twinning can be determined with good accuracy. Knowing these regions of low statistical variance should be advantageous if the twinning features are used to quantify the activity of twinning in comparison to competing deformation mechanisms. The well developed features of the two most active deformation mechanisms, basal slip and twinning, for these orientations presumably also explain the observed minimum in the orientation dependent hardness of single crystal magnesium.

It is interesting to note that Clayton and Knap [30] reported phase-field simulation results which predicted a layered twin structure growing from a large twin for wedge

indentation of calcite. These predicted patterns of lamellar twinning resemble some of the observations from this work, especially for the intermediate orientations between the $\langle c \rangle$-axis and the basal great circle.

5.6. Non-planar twin interfaces and twin-trace analysis

Trace analysis of the extension twins did not always show good alignment of the often curved twin-matrix interface with the twin plane. Similar incoherent twin boundaries were also reported by Shin et al. [72] from a cross-sectional TEM analysis of Berkovich indentations into the basal and second-order prismatic planes of magnesium. The twin boundaries of $\{10\bar{1}2\}\langle\bar{1}100\rangle$ twinning have been previously reported to readily deviate from the $\{10\bar{1}2\}$ plane traces [98,99]. Also, both the twinned material as well as the matrix around the twin are presumably undergoing significant plastic deformation by dislocation glide after the twin was formed.

5.7. Twin variant selection based on the variant's twinning strains and the expanding cavity model of indentation

It has been shown in polycrystals, that the accommodation of twins by the surrounding material can play an important role in their formation. Accommodation aspects can outweigh the Schmid-factor criterion for the selection of twin variants [56,57].

A simple model of the indentation process is developed here to clarify the twin variant selection during indentation induced twinning based on a combination of two aspects. This model is based on (1) a rough approximation of the stress state during indentation as well as (2) the eigenstrains that are associated with the formation of specific extension twin variants.

The stress state during indentation has often been described by the expanding cavity model [100,101]. In this picture a half-sphere expands isotropically inside the indented half-space. For a mechanically isotropic material this deformation results in tensile stresses along the tangential directions around the half-sphere. The radial directions that extend from the surface of the half-sphere are loaded in compression. For an isotropic material this stress field results in a corresponding strain field.

Based on the expanding cavity model an analogy can be drawn to the sheet rolling of polycrystalline magnesium. During rolling a sharp $\langle c \rangle$-axis texture develops with the resulting basal plane normals perpendicular to the plane of the rolled magnesium sheet. This texture forms through a strong twin variant selection which aligns the compressive component of the twinning strain with the direction of the height reduction. Applying this principle to the case of indentation and under the assumption of the expanding cavity model, twin variant selection should lead to the formation of specific twins around the indentation. One could assume that the twinning eigenstrain associated with the promoted variant, locally approximates the strain field of the expanding cavity model. Indeed almost all of the observed twin variants have their $\langle c \rangle$-axes approximately aligned with the radial direction from the indent, c.f. Fig. 7. This indicates that the contraction of the twinned material in the approximately perpendicular direction of the parent $\langle c \rangle$-axis might be crucial for the twin variant selection during indentation.

To investigate this variant selection process further, it is useful to visualize the potential twinning strains of all six variants around the indent. The shear produced by $\{10\bar{1}2\}\langle\bar{1}100\rangle$ extension twinning in magnesium is $\gamma\mathrm{ETw} = \frac{|(c/a)^2 - 3|}{(c/a)\sqrt{3}}$ with twinning shear, $\gamma\mathrm{ETw}$, and lattice constants, a and c [47]. Inserting magnesium's c/a ratio of 1.62 yields a twinning shear of about 0.13. This corresponds to a simple shear on the twinning plane, K_1, of about 7°.

The deformation gradient, $\boldsymbol{F}$, that describes the twinning deformation in the given orientation for a specific twin system is computed as follows. The orientation of the parent grain is given as Bunge Euler angles ($Z - X - Z$ convention). From these the orientation matrix, $\boldsymbol{g}$, of the twin can be calculated by applying an additional 180° rotation around the twin shear direction. The rotated twinning shear direction, $\boldsymbol{d} = \boldsymbol{g}\boldsymbol{d_0}$, and rotated twin plane normal, $\boldsymbol{n} = \boldsymbol{g}\boldsymbol{n_0}$, are used to calculate the Schmid matrix, $\boldsymbol{S} = \boldsymbol{d} \otimes \boldsymbol{n}$. Then the deformation gradient of the twinning process is calculated as $\boldsymbol{F} = \gamma\mathrm{ETw}\boldsymbol{S} + \boldsymbol{I}$.

It can be decomposed as $\boldsymbol{F} = \boldsymbol{R}\boldsymbol{U}$ into a rotation, $\boldsymbol{R}$, and $\boldsymbol{U}$, the right stretch tensor. The logarithmic strain of the twinning process is then $\boldsymbol{E} = \ln \boldsymbol{U}$.

An approximation of the in-plane strain is calculated by setting all entries of $\boldsymbol{F}$ with a z-component to the values of the identity matrix. This 2D deformation gradient is then used to visualize the approximate twin deformation in the indented plane of the crystal. From this 2D deformation gradient, a logarithmic plane strain $\boldsymbol{E}_{xy}$ is finally derived in the same way as described above.

The 3D deformation can be visualized as an ellipsoid, see Fig. 14. The in-plane strain can be represented by a strain ellipsis, see examples in Fig. 7. The resulting visualizations connect the identified twin systems to the compressive and tensile components of their respective twinning strain in the sample surface. Analysis of the experimental data suggests that the formation of the twin variants is
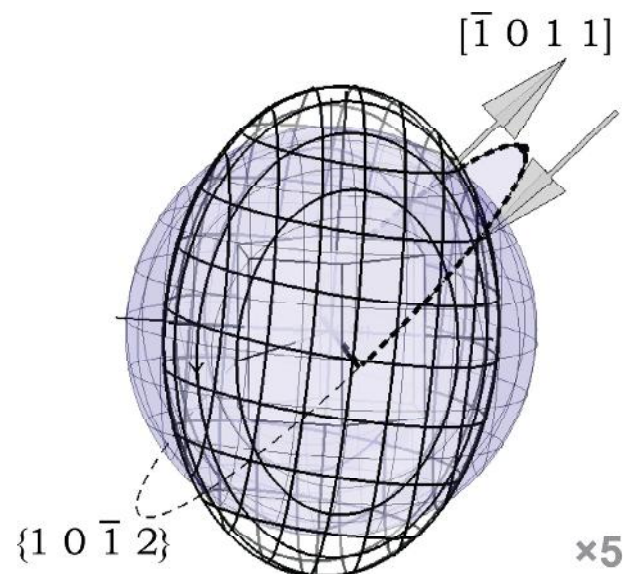

Fig. 14. Three-dimensional visualization of the strain ellipsoid of one extension twin system. The parent orientation has a $\langle c \rangle$-axis parallel to the vertical axis (z). The magnitude of the strain was multiplied by five for this visualization.

significantly influenced by the resulting in-plane deformations. Twin variants which provide extension tangential to the perimeter of the indent and at the same time compression in the approximately radial direction, are generally preferred. This is illustrated in Fig. 7c for indent 4-0-(2,3) where the identified twins either have significant tangential extension strains (twin bundles A, D), or, in addition, provide similar contraction strains in radial direction from the indent (twins B, C). This strain compatibility criterion, however, seems to be not sufficient to predict the twin variants unconditionally. While the observed variants usually have their twin strains aligned according to this guideline, the formed variants are not always the ones which agree best with this rule.

Analyzing the activated twinning variants throughout the stereographic triangle reveals different regimes for the accommodation of the twins during indentation, depending on the nature of the involved stresses. For $\langle c \rangle$-axis and intermediate indentation directions the contraction strain aligned with the radial directions from the indent seems to govern the formation of twins. The corresponding stress component is of compressive character.

The anisotropic plasticity of magnesium is best illustrated by indentation along an axis parallel to the basal great circle ($\eta \approx 90°$) such as $\langle 11\bar{2}0 \rangle$ or $\langle 10\bar{1}0 \rangle$. For these orientations the $\langle c \rangle$-axis is lying in the indented sample surface. In this case the principal stress components are compressive in the direction along the $\langle c \rangle$-axis as depicted in Fig. 12. In the regions perpendicular to the $\langle c \rangle$-axis on both sides of the indent, the principal stresses are of tensile character with their principal directions parallel to the $\langle c \rangle$-axis. The nature of these stresses is exactly as predicted by the expanding cavity model. Their magnitude, however, is locally modified by the lack of an easy mode of deformation with a $\langle c \rangle$-axis component.

5.8. Comparison of experimentally observed twin variants against CPFEM simulation results

The predicted activation of twinning variants by CPFEM partially agreed with the experimentally observed twinning patterns. In many cases, the location of volumes deformed by twin-type shear in the simulations was connected to the observation of surface-connected twin stacks around that location. However, shear activity was regularly predicted for more twinning systems than experimentally observed. For example, the near-basal ($\eta = 13°$) orientation of indent 4-0-(2,1) showed significant shearing on the T1 extension twinning system, see Figs. 7a and 11a. While the EBSD measurement did not reveal any T1 twinning at the surface, the topographic profile indicates activity of a deformation system in this location. This upheaval, however, could result from basal $\langle a \rangle$-glide as well as it could be a hint to subsurface twinning.

Another example where twinning activity was over-predicted in the simulations are the simulated shear distributions for indent 4-0-2,3 (green ND-IPF coloring). The simulations were performed based on the Euler angles according to the in-plane orientation convention, c.f. Table A.4. The CPFEM simulations predicted activity of twinning systems in pairs (T1/T4 and T3/T6) and in strongly overlapping locations, see Fig. 11c. The twin shear of variant T3 that was observed in the experiments (c.f. Fig. 7c, twin bundle "A", located above the indent) transports material on the side closer to the indent into the

sample, and on the side of the twinning plane away from the indent it points out of the sample surface. This is in agreement with the schematic in Fig. 13. For the other twin variant, T6, that was predicted by CPFEM, a similar configuration cannot exist at this location because its twin habit plane is not tangentially aligned with the indent, see Fig. 7c. Additionally, its twin shear direction is directed approximately parallel to the normal on the indenter surface, i.e. in a radial direction with respect to the indent.

For the experimentally observed twin stack below indent 4-0-(2,3) in Fig. 11d ("D" in Fig. 7c, T4) the configuration is similar. One instance of activation of the complementary system (T1) was observed by EBSD for indent 4-0-(7,2), see Fig. 5. Indent 4-0-(7,2) has an almost identical indentation axis just 2.3° from indent 4-0-(2,3). The location of the activated variant T1 is not exactly corresponding to the region where the CPFEM simulations predicted the highest shear on that system. The twin lamellae of system T1 were observed shifted to the right, where the twin shear is again aligned with the impression in a roughly tangential fashion. At the same time only three instead of five twin lamellae were formed and the twinned area was smaller for this variant, T1, than observed for variant T4 in indent 4-0-(2,3).

Simultaneous activation of two or more twin variants in the same location was not observed in the experiments. It is assumed that in reality always one of the twin variants is preferred by the specific local conditions. Also it is possible that the formation of the first twin lath modifies the local stress field such that the nucleation or growth of other twin variants is suppressed.

It has been stated in the literature that the selection of twin variants does not strictly obey the Schmid law [19,20]. However, this deviation from the Schmid law is usually derived from polycrystal experiments, where Schmid-factors are often estimated based on the global stress state. Without analysis of the full stress fields these findings have to be taken into account only while keeping in mind this coarse and for magnesium even problematic assumption that the local stresses can be approximated by the macroscopic volume-averaged stress on the polycrystal. Here, all of the experimentally observed twinning variants showed significant resolved shear stresses in the 3D CPFEM simulations. However, some of the variants that were predicted by CPFEM could not be observed in the experiments. Thus a non-zero resolved shear stress for a specific twinning system seems to be a necessary but not sufficient condition for the nucleation or growth of this variant. This is in agreement with previous findings in polycrystalline magnesium, where the ease of accommodation of the twinning strain by deformation of adjacent grains led to similar twin variant selection [57].

Further, regarding the prediction of twin variants by CPFEM that were not experimentally observed, it is conceivable that the simulated concurrent activation of more than one twin variant in a similar region is an artifact of the specific implementation of the constitutive law. In the presence of unidirectional pseudo-twin shear systems, the most efficient way of accommodating the imposed deformation could be to activate two systems simultaneously in order to reduce the accommodation requirements on the surrounding matrix. The observation of complementary twin-shear in the simulations would then be a result of the approximation of the twin deformation by unidirectional slip systems. Without taking into account the formation of twin interfaces and reorientation of the lattice, these

additional "phantom" modes of twin-like deformation are not hindered like in the real material but might even be promoted by the backstress of the surrounding matrix onto the "twinned" volume. Possibly these modes could be suppressed by setting an artificially high value for the cross-hardening of twin systems that shear in a common plane. Alternatively, orientations of material points could be flipped into the twin orientation after a certain threshold of twin-like shear deformation. However, from these phenomenological approaches no satisfying explanation of the twin microstructures and other details of the experiments can be expected. Therefore, the realistic simulation of the twin patterning is left for improved modeling approaches that achieve a more physical description of the twinning process.

Molecular dynamic (MD) simulation could help to reproduce the observed twin morphologies while at the same time the presented experimental data might be used to tune the model parameters such as the embedded atom potentials of the simulations. However, the computational effort following from the length and time scale of our experiments is still prohibitive for an MD approach. Nevertheless, MD simulations could help to clarify the questions about when, where and how individual twins are nucleated during the initial stages of the indentation.

Because phase-field modeling has already been successfully applied to reproduce twinning microstructures [30], this technique seems to be promising for future simulation efforts. The observed twinning microstructures around indents are especially suited to validate improved modeling approaches because of the characteristic twin morphologies.

5.9. Comparison with the indentation response of other hexagonal metals

5.9.1. Titanium

It is interesting to compare the orientation dependent indentation of magnesium to the response of other hexagonal close packed metals. Zambaldi et al. [70] presented the orientation dependent pile-up response of alpha-titanium during indentation of individual grains with a sphero-conical indenter. Indentation of titanium away from the $\langle c \rangle$-axis leads to the formation of two pile-up lobes on both sides of the projection of the $\langle c \rangle$-axis onto the sample surface. Consequently, for these orientations, the maximum pile-up in titanium is observed exactly in the locations of maximum sink-in for magnesium. For indentation of titanium along the [0 0 0 1] axis virtually no pile-up was observed, whereas significant pile-up is formed in magnesium for that indentation direction.

No twinning was detected in titanium for any of the indented orientations. Cross-sectional TEM analysis of similar indents in a hexagonal Ti–7Al (wt.%) alloy only showed one instance of a possible extension twin of type $\{10\bar{1}2\}\langle\bar{1}100\rangle$ [102].

5.9.2. Comparison to indentation of beryllium at room and elevated temperature

It is expected that the indentation response of magnesium will change significantly with changes in temperature or chemical composition. The work of Tsuya [65] on indentation of beryllium is an example of what kind of effects could be expected. Tsuya [65] conducted these experiments with Knoop and Vickers tools. However, the observed indent microstructures seem to be remarkably robust against variation of the indenter shape. Also, in most cases the faces of the indenter were aligned with crystallographic directions in order to minimize the additional anisotropy introduced by the tool geometry.

Depending on the temperature during indentation, beryllium closely resembles the room temperature behavior of either magnesium or titanium. At room temperature Beryllium shows predominantly basal slip and twinning as observed for magnesium in the present study [65, Fig. 9 a, b, d]. At a temperature of 300 °C, indentations perpendicular to the $\langle c \rangle$-axis into the $(10\bar{1}0)$ prism plane [65, Fig. 9c] show slip patterns that are analog to the deformation by prismatic $\langle a \rangle$-glide in Ti$_3$Al [103], pure titanium [70], and Ti–7Al (wt.%) [102] as described above.

5.10. Advantages and drawbacks of the presented conical indentation method

A specific advantage of the sharp conical indentation as presented here is the geometrical self-similarity of the remaining impressions. This self-similarity facilitates quantitative comparisons of different series of experiments which might produce variable absolute dimensions of the indents. Experimental findings can be re-scaled and compared over a range of indent sizes as long as size effects do not introduce an additional dependency.

Another advantage of the method is that careful interpretation of the load–displacement curve will reveal the conditions at which twinning was initiated. During displacement-controlled indentation a sudden load–drop indicates the nucleation and growth of a twin; in load-controlled indentation a jump in the displacement marks twinning events on the curve.

The perhaps most prominent advantage of the indentation-based analysis of deformation mechanisms is its efficiency. The use of automated microindentation in combination with confocal microscopy measurement of the topographies is efficient in comparison to fully automated nanoindentation coupled with atomic force microscopy (AFM) characterization. Additionally, the acquisition time for optical topography measurements is reduced in comparison to AFM characterization. An improvement over nano-scale indentation is the availability of microindenters with good geometry conformance. In combination with crystal orientation mapping, many orientations can be probed for their single-phase micromechanical behavior. Also, due to the probing of random orientations in a polycrystal for their indentation response, the tedious preparation of single crystals of specific orientations is not necessary. A detailed analysis of individual orientations can be readily performed, but also the full orientation dependency of the observed phenomena can be efficiently characterized.

A general drawback of indentation testing is that currently there exists no approach to extend it to non-monotonous cyclic loading. Another shortcoming is that due to the complex loading during indentation a detailed understanding of the deformation process can only be gained by 3D simulations with adequate constitutive laws.

One aspect of indentation has positive as well as detrimental effects on its application to study the single crystal plasticity of magnesium: the strong confinement of the deformed volume by the surrounding material. On the one hand this confinement leads to an increased hydrostatic stress in the plastic zone and thus might influence the

activation of deformation mechanisms. On the other hand, it largely prevents the strong localization of the deformation on the basal plane as it is observed for example in uniaxial compression or tensile testing as discussed below.

5.11. Comparison with other approaches to characterize the single crystal micromechanics of magnesium

The channel die technique [39,104,41] aims to impose homogeneous plane strain compression on the sample. The strong localization of plastic deformation by twinning, however, prevents this objective from being achieved since a single twin will introduce significant heterogeneity into the deformation field.

The same applies to deformation of micropillars [42,18,43] where the high localization of basal slip frequently changes the sample's geometry to such extent that the homogeneous stress assumption is violated. Without taking into account the 3D deformation of the pillar only the stress state at the very initial stages of the deformation can be estimated.

From the above arguments it is clear that no single kind of deformation experiment is able to capture all facets of the plastic deformation of magnesium and each technique has specific benefits.

6. Conclusions

A recently developed combination of experimental and computational techniques to investigate the activation of plastic deformation mechanisms by indentation was adapted to the case of a hexagonal metal that exhibits easy activation of twinning. The following core characteristics and interpretations were found:

(a) Profuse extension twinning was observed on the surface surrounding conical indents in magnesium crystals of any orientation.

(b) The twinning microstructures around indentations are a strong function of the indented orientation.

(c) In magnesium, specific extension twinning variants can be reproducibly activated by indentation and in well-defined locations relative to the indent.

(d) The twins mostly form in a lamellar fashion with the twin ledge widths and spacings nearly independent of the final size of the indent.

(e) The observed patterns for specific indented orientations were fairly reproducible with orientation-dependent levels of statistical variation.

(f) The activation of specific twinning variants cannot be interpreted solely based on the resolved shear stress acting for that system. An accommodation criterion has to be taken into account additionally. Significant resolved shear stress acting on extension twinning systems, as well as a twinning strain which is compatible with the imposed deformation, are necessary criteria for the growth of specific twin variants.

(g) The expanding cavity model of indentation together with the three-dimensional twinning strains, seems to be useful to understand twin variant selection during indentation in magnesium despite magnesium's extreme plastic anisotropy.

(h) Sharp conical indenter geometries can provide reproducible and comparable data on the predominant plastic deformation mechanisms of ductile metals. Comparison with the indentation behavior of other metals emphasizes the characteristic nature of the indent patterns. In magnesium these patterns directly reflect the activity of basal ⟨a⟩-glide and extension twinning at room temperature.

The presented inverse pole figure of indent microstructures can be used as a quick and convenient reference for the identification of the relative activation of deformation systems. The availability of such a controlled and fast method to check for the operating slip and twinning systems will hopefully promote the alloy optimization.

7. Outlook

With small adaptations, the technique used in this study might also be extended to related issues, some of which are discussed below. The method might for example be used to study the details of plastic accommodation and intersection of twins [105–107] under controlled conditions. The latter could be achieved by placing two indents within a small distance such that the emerging twins from the second indent will intersect with the preexisting twin laths from the first indent. Alternatively, specific twin variants could be induced in the vicinity of larger preexisting twins, to make them intersect.

Three-dimensional microstructural characterization of the indent microstructures will help to consolidate the understanding of the deformation during indentation of magnesium. Especially investigations of the early stage of deformation could clarify the nucleation mechanisms of the twin lamellae.

A detailed analysis of the twinning microstructures could analyze the orientation and size dependence of the twin microstructures together with their statistical variations. Ideally, it would also quantify these aspects separately for the individual twinning variants. Another open question is whether the distances and widths of the observed twin stacks depend on the material's history or whether they are an intrinsic and thus stable property of the nucleation and growth processes for twinning in magnesium.

Improved quantifications of the indent microstructures will enable comparative studies of the indentation response for room and elevated temperatures and for different chemical compositions, as well as for the indentation of other hexagonal metals and alloys. It is expected that experiments for different compositions or temperatures will lead to significant changes in the respective measures and will allow useful conclusions about the temperature dependence of the activated deformation mechanisms.

Additionally, in experiments not reported here, the nucleation of a twin from the grain boundary could be triggered by placing an indent close to a grain boundary. This observation could help to clarify the mechanisms by which twinning in polycrystalline magnesium is nucleated at the grain boundaries [108].

Presumably, experiments analogous to twinning in magnesium could also be carried out to study phase transformation processes such as the formation of strain-induced martensite [109].

Table A.4. Full crystallographic orientations for indentations discussed in the text. The first column contains the indent label, the second one the Bunge Euler angles (BEA) as measured by EBSD. The third and fourth column contains the Euler angles and spherical polar angles after conversion according to the in-plane orientation convention [75]. The last two columns list the Miller–Bravais direction indices of the respective indentation axes and the in-plane rotation angle to convert between the experimental orientations and the orientations after the convention.

Indent	EBSD $\varphi_1, \Phi, \varphi_2$ (°)	BEA (°), conv.	ζ, η (°)	[$uvtw$]	Rot. (°)
1-2-4	(153.0 35.7 195.1)	(284.9 35.7 75.1)	14.9, 35.7	[$7\bar{2}\bar{5}9$]	131.9
1-3-3	(243.5 34.1 98.3)	(321.7 34.1 38.3)	51.7, 34.1	[$53\bar{8}11$]	78.2
1-3-7	(205.1 49.5 183.5)	(296.5 49.5 63.5)	26.5, 49.5	[$14\bar{1}\bar{13}12$]	91.4
1-6-11	(72.4 14.2 278.1)	(321.9 14.2 38.1)	51.9, 14.2	[$21\bar{3}11$]	249.5
3-1-4	(242.0 84.7 126.8)	(293.2 84.7 66.8)	23.2, 84.7	[$21\bar{3}\bar{1}82$]	51.2
3-1-27	(13.1 40.2 346.4)	(313.6 40.2 46.4)	43.6, 40.2	[$62\bar{8}9$]	300.5
3-1-41	(144.4 58.0 196.5)	(283.5 58.0 76.5)	13.5, 58.0	[$10\bar{3}\bar{7}6$]	139.1
4-0-2,1	(185.9 13.0 161.4)	(318.6 13.0 41.4)	48.6, 13.0	[$21\bar{3}12$]	132.7
4-0-2,3	(184.8 74.1 204.5)	(275.5 74.1 84.5)	5.5, 74.1	[$12\bar{5}\bar{7}3$]	90.7
4-0-2,4	(130.8 74.8 210.6)	(329.5 74.8 30.6)	59.5, 74.8	[$22\bar{4}1$]	198.6
4-0-3,6	(181.2 87.1 192.1)	(287.9 87.1 72.1)	17.9, 87.1	[$18\bar{4}\bar{14}1$]	106.7
4-0-2,10	(158.9 42.0 203.4)	(276.6 42.0 83.4)	6.6, 42.0	[$5\bar{2}\bar{3}5$]	117.7
4-0-2,12	(270.0 24.1 119.5)	(300.6 24.1 59.5)	30.6, 24.1	[$30\bar{3}7$]	29.7
4-0-4,7	(188.4 87.0 197.6)	(282.5 87.0 77.6)	12.5, 87.0	[$16\bar{5}\bar{11}1$]	94.0
4-0-5,2	(1.1 82.0 18.7)	(281.3 82.0 78.7)	11.3, 2.0	[$15\bar{5}\bar{10}2$]	280.2
4-0-6,5	(168.1 67.0 178.3)	(301.7 67.0 58.3)	31.7, 67.0	[$191\bar{20}9$]	133.6
4-0-6,11	see 4-0-7,9				
4-0-7,9	(37.7 61.4 338.7)	(321.3 61.4 38.7)	51.3, 61.4	[$53\bar{8}4$]	283.6
5-1-12	(313.7 85.4 32.1)	(327.9 85.4 32.1)	57.9, 85.4	[$76\bar{13}1$]	14.2
5-5-12	(222.7 79.4 130.2)	(289.8 79.4 70.2)	19.8, 79.4	[$11\bar{2}\bar{9}2$]	67.1

Acknowledgements

Appendix A. Extension twinning systems

The numbering of the $\{10\bar{1}2\}\langle\bar{1}100\rangle$ extension twinning systems of magnesium is given in Table A.3.

Appendix B. Orientation data

The full orientations, as measured by EBSD, of a number of indent locations are given in Table A.4. For a detailed description about the applied in-plane rotation convention (third column) see Zambaldi Raabe [75] and the calculation tool at http://zambaldi.de/sx-indent.

References

[1] I. Polmear, Light alloys: From Traditional Alloys to Nanocrystals, Fourth ed., Butterworth-Heinemann (Elsevier), 2006.

[2] S. Agnew, J. Nie, Scripta Mater. 63 (7) (2010) 671–673.

[3] C. Bettles, M. Barnett (Eds.), Advances in Wrought Magnesium Alloys: Fundamentals of Processing, Properties and Applications, Woodhead Publishing, Oxford, UK, 2012.

[4] J. Hirsch, T. Al-Samman, Acta Mater. 61 (3) (2013) 818–843.

[5] S. Ando, H. Tonda, Mater. Sci. Forum 350–351 (2000) 43–48.

[6] S. Agnew, M. Yoo, C. Tomé, Acta Mater. 49 (20) (2001) 4277–4289.

[7] S.R. Agnew, J.A. Horton, M.H. Yoo, Metall. Mater. Trans. A 33 (3) (2002) 851–858.

[8] M. Barnett, M. Nave, C. Bettles, Mater. Sci. Eng. A 386 (1–2) (2004) 205–211.

[9] J. Bohlen, M.R. Nïnberg, J.W. Senn, D. Letzig, S.R. Agnew, Acta Mater. 55 (6) (2007) 2101–2112.

[10] S. Sandlöbes, S. Zaefferer, I. Schestakow, S. Yi, R. Gonzalez-Martinez, Acta Mater. 59 (2) (2011) 429–439.

[11] C. Boehlert, Z. Chen, A. Chakkedath, I. Gutiérrez-Urrutia, J. Llorca, J. Bohlen, S. Yi, D. Letzig, M. Pérez-Prado, Philos. Mag. 93 (6) (2013) 598–617.

[12] S. Sandlöbes, Z. Pei, M. Friák, L.F. Zhu, F. Wang, S. Zaefferer, D. Raabe, J. Neugebauer, Acta Mater. 70 (2014) 92–104.

[13] F. Wang, S. Sandlöbes, M. Diehl, L. Sharma, F. Roters, D. Raabe, Acta Mater. 80 (2014) 77–93.

[14] D.R. Steinmetz, T. Jäpel, B. Wietbrock, P. Eisenlohr, I. Gutierrez-Urrutia, A. Saeed-Akbari, T. Hickel, F. Roters, D. Raabe, Acta Mater. 61 (2) (2013) 494–510.

[15] J.A. Yasi, T. Nogaret, D.R. Trinkle, Y. Qi, L.G. Hector, W.A. Curtin, Modell. Simul. Mater. Sci. Eng. 17 (5) (2009) 055012.

[16] J. Wang, I. Beyerlein, C. Tomé, Int. J. Plast. (2013).

[17] B. Syed, J. Geng, R. Mishra, K. Kumar, Scripta Mater. 67 (7–8) (2012) 700–703.

[18] G.S. Kim, Small volume investigation of slip and twinning in magnesium single crystals. Ph.D. thesis, Université de Grenoble, 2011.

[19] J. Wang, I. Beyerlein, C. Tomé, Scripta Mater. 63 (7) (2010) 741–746.

[20] I. Beyerlein, L. Capolungo, P. Marshall, R. McCabe, C. Tomé, Philos. Mag. 90 (16) (2010) 2161–2190.

[21] J.H. Brunton, M.P.W. Wilson, Proc. Roy. Soc. London A 309 (1498) (1969) 345–361.

[22] R. Glüge, A. Bertram, T. Böhlke, E. Specht, ZAMM 90 (7–8) (2010) 565–594.

[23] J. Zhang, S.P. Joshi, J. Mech. Phys. Solids 60 (5) (2012) 945–972.

[24] H. Abdolvand, M.R. Daymond, J. Mech. Phys. Solids 61 (3) (2013) 803–818.

[25] S. Graff, W. Brocks, D. Steglich, Int. J. Plast. 23 (12) (2007) 1957–1978.

[26] J. Mosler, M. Homayonifar, GAMM-Mitteilungen 35 (1) (2012) 43–58.

[27] H. Wang, P. Wu, J. Wang, C. Tomé, Int. J. Plast. 49 (2013) 36–52.

[28] A. Oppedal, H. El Kadiri, C. Tomé, S.C. Vogel, M. Horstemeyer, Philos. Mag. 35 (2013) 4311–4330.

[29] S. Hu, C.H. Henager, L. Chen, Acta Mater. 58 (19) (2010) 6554–6564.

[30] J.D. Clayton, J. Knap, Modell. Simul. Mater. Sci. Eng. 19 (8) (2011) 085005.

[31] J. Clayton, J. Knap, Acta Mater. 61 (14) (2013) 5341–5353.

[32] V.I. Levitas, A.M. Roy, D.L. Preston, Phys. Rev. B 88 (5) (2013).

[33] K. Máthis, K. Nyilas, A. Axt, I. Dragomir-Cernatescu, T. Ungár, P. Lukáč, Acta Mater. 52 (10) (2004) 2889–2894.

[34] L. Balogh, S. Niezgoda, A. Kanjarla, D. Brown, B. Clausen, W. Liu, C. Tomé, Acta Mater. 61 (10) (2013) 3612–3620.

[35] J. Lind, S. Li, R. Pokharel, U. Lienert, A. Rollett, R. Suter, Acta Mater. 76 (2014) 213–220.

[36] A. Fernández, A. Jèrusalem, I. Gutiérrez-Urrutia, M. Pérez-Prado, Acta Mater. 61 (20) (2013) 7679–7692.

[37] E. Schmid, Z Elektrochem. Angew. Phys. Chem. 37 (1931) 447–459.

[38] A. Akhtar, E. Teghtsoonian, Philos. Mag. 25 (4) (1972) 897–916.

[39] E. Kelley, W. Hosford, Trans. Metall. Soc. AIME 242 (1968) 5–13.

[40] A. Chapuis, J.H. Driver, Acta Mater. 59 (5) (2011) 1986–1994.

[41] T. Al-Samman, K.D. Molodov, D.A. Molodov, G. Gottstein, S. Suwas, Acta Mater. 60 (2) (2012) 537–545.

[42] E. Lilleodden, Scripta Mater. 62 (8) (2010) 532–535.

[43] C.M. Byer, K. Ramesh, Acta Mater. 61 (10) (2013) 3808–3818.

[44] B. Wonsiewicz, W. Backofen, Trans. Metall. Soc. AIME 239 (9) (1967) 1422–1431.

[45] W. Hutchinson, M. Barnett, Scripta Mater. 63 (7) (2010) 737–740.

[46] W.J.M. Tegart, Philos. Mag. 9 (98) (1964) 339–341.

[47] M.H. Yoo, Metall. Trans. A 12 (3) (1981) 409–418.

[48] J. Stohr, J. Poirier, Philos. Mag. 25 (6) (1972) 1313.

[49] I. Jones, W. Hutchinson, Acta Metall. 29 (6) (1981) 951–968.

[50] J.W. Christian, S. Mahajan, Progr. Mater. Sci. 39 (1–2) (1995) 1–157.

[51] C. Aydiner, J. Bernier, B. Clausen, U. Lienert, C. Tomé, D. Brown, Phys. Rev. B 80 (2) (2009).

[52] C. Barrett, H. El Kadiri, M. Tschopp, J. Mech. Phys. Solids 60 (12) (2012) 2084–2099.

[53] Q. Yu, Z. Shan, J. Li, X. Huang, L. Xiao, J. Sun, E. Ma, Nature 463 (7279) (2010) 335–338.

[54] H. ElKadiri, J. Kapil, A. Oppedal, L. Hector, S.R. Agnew, M. Cherkaoui, S. Vogel, Acta Mater. 61 (10) (2013) 3549–3563.

[55] E. Martin, L. Capolungo, L. Jiang, J. Jonas, Acta Mater. 58 (11) (2010) 3970–3983.

[56] J.J. Jonas, S. Mu, T. Al-Samman, G. Gottstein, L. Jiang, E. Martin, Acta Mater. 59 (5) (2011) 2046–2056.

[57] S. Mu, J.J. Jonas, G. Gottstein, Acta Mater. 60 (5) (2012) 2043–2053.

[58] S. Wang, C. Schuman, L. Bao, J. Lecomte, Y. Zhang, J. Raulot, M. Philippe, X. Zhao, C. Esling, Acta Mater. 60 (9) (2012) 3912–3919.

[59] Y. Pei, A. Godfrey, J. Jiang, Y. Zhang, W. Liu, Q. Liu, Mater. Sci. Eng. A 550 (2012) 138–145.

[60] I.J. Beyerlein, C.N. Tomé, Proc. Roy. Soc. A 466 (2121) (2010) 2517–2544.

[61] G. Tammann, A. Müller, Z. Metall. 18 (1926) 69–79.

[62] R. Reed-Hill, W. Robertson, Acta Metall. 5 (12) (1957) 728–737.

[63] P. Partridge, E. Roberts, Acta Metall. 12 (11) (1964) 1205–1210.

[64] M.H. Yoo, C.T. Wei, J. Appl. Phys. 38 (1967) 2974–2976.

[65] K. Tsuya, J. Nucl. Mater. 22 (2) (1967) 148–157.

[66] R.C. Blish, J. Appl. Phys. 39 (5) (1968) 2290.

[67] J.H. Cho, S.H. Kim, S.H. Han, S.B. Kang, Microsc. Microanal. 19 (S5) (2013) 8–12.

[68] S. Basu, M.W. Barsoum, J. Mater. Res. 22 (09) (2007) 2470–2477.

[69] S. Basu, M. Radovic, M. Barsoum, J. Appl. Phys. 104 (6) (2008).

[70] C. Zambaldi, Y. Yang, T.R. Bieler, D. Raabe, J. Mater. Res. 27 (01) (2012) 356–367.

[71] H. Somekawa, C.A. Schuh, Scripta Mater. 68 (6) (2013) 416–419.

[72] J.H. Shin, S.H. Kim, T. Ha, K. Oh, I.S. Choi, H. Han, Scripta Mater. 68 (7) (2013) 483–486.

[73] H. Kitahara, T. Mayama, K. Okumura, Y. Tadano, M. Tsushida, S. Ando, Acta Mater. 78 (2014) 290–300.

[74] B. Selvarajou, J.H. Shin, T.K. Ha, Is. Choi, S.P. Joshi, H.N. Han, Acta Mater. 81 (2014) 358–376.

[75] C. Zambaldi, D. Raabe, Acta Mater. 58 (9) (2010) 3516–3530.

[76] Y. Wang, D. Raabe, C. Klüber, F. Roters, Acta Mater. 52 (8) (2004) 2229–2238.

[77] N. Zaafarani, D. Raabe, R.N. Singh, F. Roters, S. Zaefferer, Acta Mater. 54 (7) (2006) 1863–1876.

[78] C. Zambaldi, F. Roters, D. Raabe, U. Glatzel, Mater. Sci. Eng. A 454 (2007) 433–440.

[79] H. Chang, M. Fivel, D. Rodney, M. Verdier, C. R. Phys. 11 (3–4) (2010) 285–292.

[80] F. Roters, P. Eisenlohr, L. Hantcherli, D.D. Tjahjanto, T.R. Bieler, D. Raabe, Acta Mater. 58 (4) (2010) 1152–1211.

[81] B. Eidel, Acta Mater. 59 (4) (2011) 1761–1771.

[82] D. Mercier, C. Zambaldi, T.R. Bieler, Proc. ICOTOM17 2014; preprint, doi:wv4.

[83] R.S. Kalidindi, A.C. Bronkhorst, L. Anand, J. Mech. Phys. Solids 40 (3) (1992) 537–569.

[84] F. Roters, P. Eisenlohr, C. Kords, D. Tjahjanto, M. Diehl, D. Raabe, Proc. IUTAM 3 (2012) 3–10.

[85] F. Roters et al. Düsseldorf Advanced MAterials Simulation Kit – DAMASK.mpie.de. 2011.

[86] S. Kalidindi, J. Mech. Phys. Solids 46 (2) (1998) 267–290.

[87] G. Simmons, H. Wang, Single Crystal Elastic Constants and Calculated Aggregate Properties: A Handbook, MIT Press, Cambridge, MA, 1971.

[88] Kitware Inc., Paraview (http://paraview.org). 2013.

[89] C. Zambaldi, F. Roters, D. Raabe, Intermetallics 19 (6) (2011) 820–827.

[90] A. Serra, D.J. Bacon, R.C. Pond, Metall. Mater. Trans. A 33 (3) (2002) 809–812.

[91] P.M. Sargent, T.F. Page, J. Mater. Sci. 20 (7) (1985) 2388–2398.

[92] R. Hill, F. Storakers, A. Zdunek, Proc. R. Soc. Lond. A 423 (1989) 301–330.

[93] B.J. Hockey, J. Am. Ceram. Soc. 54 (5) (1971) 223–231.

[94] J. Holden, Philos. Mag. 43 (344) (1952) 976–984.

[95] A. Moore, Acta Metall. 3 (2) (1955) 163–169.

[96] H. Yoshinaga, R. Horiuchi, Trans. JIM 4 (1963) 1–8.

[97] W. Poole, G. Nayyeri, C. Sinclair, personal communication, 2014.

[98] X. Zhang, B. Li, X. Wu, Y. Zhu, Q. Ma, Q. Liu, P. Wang, M. Horstemeyer, Scripta Mater. 67 (10) (2012) 862–865.

[99] A. Ostapovets, P. Molnár, Scripta Mater. 69 (4) (2013) 287–290.

[100] Fischer-Cripps, Introduction to Contact Mechanics, Second ed., Springer, 2007.

[101] K.L. Johnson, J. Mech. Phys. Solids 18 (2) (1970) 115–126.

[102] J. Kwon, M. Brandes, M. Brandes, P. Sudharshan Phani, A. Pilchak, Y. Gao, E. George, G. Pharr, M. Mills, Acta Mater. 61 (13) (2013) 4743–4756.

[103] C. Zambaldi, Micromechanical modeling of gamma-TiAl based alloys. Ph.D. thesis, RWTH Aachen, 2010.

[104] P. Šedá, A. Ostapovets, A. Jäger, P. Lejček, Philos. Mag. 92 (10) (2012) 1223–1237.

[105] E. Roberts, P.G. Partridge, Acta Metall. 14 (4) (1966) 513–527.
[106] S. Yi, I. Schestakow, S. Zaefferer, Mater. Sci. Eng. A 516 (1–2) (2009) 58–64.
[107] M.R. Barnett, N. Stanford, A. Ghaderi, F. Siska, Acta Mater. 61 (20) (2013) 7859–7867.

[108] L. Wang, P. Eisenlohr, Y. Yang, T.R. Bieler, M.A. Crimp, Scripta Mater. 63 (8) (2010) 827–830.
[109] T.H. Ahn, S.B. Lee, K.T. Park, K.H. Oh, H.N. Han, Mater. Sci. Eng. A 598 (2014) 56–61.